CONTINUOUS MID-INFRARED STAR FORMATION RATE INDICATORS: DIAGNOSTICS FOR 0 < z < 3 STAR-FORMING GALAXIES

A. J. Battisti[1], D. Calzetti[1], B. D. Johnson[2], AND D. Elbaz[3]

[1] Department of Astronomy, University of Massachusetts, Amherst, MA 01003, USA; abattist@astro.umass.edu
[2] Harvard-Smithsonian Center for Astrophysics, 60 Garden Street, Cambridge, MA 02138, USA
[3] Laboratoire AIM-Paris-Saclay, CEA/DSM/Irfu, CNRS, Université Paris Diderot, Saclay, pt courrier 131, F-91191 Gif-sur-Yvette, France

ABSTRACT

We present continuous, monochromatic star formation rate (SFR) indicators over the mid-infrared wavelength range of 6–70 μm. We use a sample of 58 star-forming galaxies (SFGs) in the *Spitzer*–SDSS–*GALEX* Spectroscopic Survey at $z < 0.2$, for which there is a rich suite of multi-wavelength photometry and spectroscopy from the ultraviolet through to the infrared. The data from the *Spitzer* Infrared Spectrograph (IRS) of these galaxies, which spans 5–40 μm, is anchored to their photometric counterparts. The spectral region between 40–70 μm is interpolated using dust model fits to the IRS spectrum and *Spitzer* 70 and 160 μm photometry. Since there are no sharp spectral features in this region, we expect these interpolations to be robust. This spectral range is calibrated as a SFR diagnostic using several reference SFR indicators to mitigate potential bias. Our band-specific continuous SFR indicators are found to be consistent with monochromatic calibrations in the local universe, as derived from *Spitzer*, *WISE*, and *Herschel* photometry. Our local composite template and continuous SFR diagnostics are made available for public use through the NASA/IPAC Infrared Science Archive (IRSA) and have typical dispersions of 30% or less. We discuss the validity and range of applicability for our SFR indicators in the context of unveiling the formation and evolution of galaxies. Additionally, in the era of the *James Webb Space Telescope* this will become a flexible tool, applicable to any SFG up to $z \sim 3$.

Key words: galaxies: star formation – infrared: galaxies – stars: formation

1. INTRODUCTION

Star formation is a fundamental parameter of galaxies that describes how galaxies evolve, when used in conjunction with mass. As the process of star formation depletes a galaxy of its gas, it must be continuously replenished by infall from the intergalactic medium to be supported for an extended time. When massive stars die, they enrich the surrounding interstellar medium with heavy metals, thus altering a galaxy's chemical composition. Therefore, accurately tracing star formation though cosmic time gives key constraints on how galaxies are able to form and evolve (e.g., Tinsley 1968; Somerville et al. 2012; Madau & Dickinson 2014, and references therein).

For these reasons, great efforts have been made to calibrate a wide range of the electromagnetic spectrum that can be linked to processes involved with recent star formation (see the review by Kennicutt & Evans 2012). In particular, infrared (IR) wavelength calibrations are proving to be critical to understanding galaxies in the early universe. Deep IR surveys with the *Spitzer* and *Herschel* Space Telescopes have revealed that the majority of star formation that occurs at redshift $z \sim 1$–3 is enshrouded by dust (e.g., Murphy et al. 2011a; Elbaz et al. 2011), making it very difficult to measure accurate star formation rates (SFRs) at optical wavelengths. In addition, IR-bright galaxies ($L \gtrsim \times 10^{11} L_\odot$) are much more prevalent during that time than today (e.g., Chary & Elbaz 2001; Le Floc'h et al. 2005; Magnelli et al. 2009; Murphy et al. 2011a; Elbaz et al. 2011; Lutz 2014, and references therein). Furthermore, observations suggest that ∼85% of today's stars were formed at redshift $0 < z < 2.5$ (Marchesini et al. 2009; Muzzin et al. 2013; Tomczak et al. 2014). Together these results have renewed interest in monochromatic (i.e., single-band) mid-IR (MIR) SFR indicators, as distant galaxies can easily be observed in the MIR.

Dust emission in the MIR is more closely related to star formation than longer IR wavelengths, where heating by low mass (i.e., long-living) stars becomes important, which has allowed several wavelength bands in the MIR to be well calibrated locally as SFR diagnostics (Zhu et al. 2008; Rieke et al. 2009; Calzetti et al. 2010). However, difficulties arise in utilizing local calibrations because the regions of rest-frame wavelengths probed by a given band will vary with redshift. As a reference, the *Spitzer* 24 μm and the *Herschel* 70 μm bands target the rest-frame 8 and 23 μm emission, respectively, for a galaxy at redshift $z = 2$. Correcting for this effect is most commonly achieved through k-corrections which depend heavily on the assumed galaxy spectral energy distribution (SED) template. Such templates (e.g., Chary & Elbaz 2001; Dale & Helou 2002; Polletta et al. 2007; Rieke et al. 2009; Brown et al. 2014) typically require many photometric bands for accurate matching. Therefore, in order to fully utilize current and future deep IR imaging surveys for a greater understanding the formation and evolution of galaxies without a reliance on extensive multi-band imaging, continuous single-band SFR indicators will be imperative.

In the near future, the Mid-Infrared Instrument (MIRI; 5–28 μm) on board the *James Webb Space Telescope* (*JWST*) will expand our ability to probe galaxies in the MIR, detecting down to the regime of normal star-forming disk galaxies ($L \lesssim 3 \times 10^{11} L_\odot$) out to $z = 3$ and representing an order of magnitude improvement in sensitivity over *Spitzer* bands of similar wavelength.[4] Thus, current and future cosmological surveys are highlighting the need for continuous monochromatic SFR indicators that cover, without breaks, the MIR wavelength range of 6–70 μm. This will provide a flexible tool

---

[4] http://stsci.edu/jwst/instruments/miri/instrumentdesign/filters/

that can be applied to any galaxy up to redshift $z \approx 3$. With the release of the Wide-field Infrared Survey Explorer (*WISE*) All-Sky Survey (Wright et al. 2010), times are ripe for consolidating all these data into a coherent picture. In this study, we use *GALEX*, Sloan Digital Sky Survey (SDSS), *WISE*, and *Spitzer* data of a large sample of local galaxies to perform the calibration of SFR(λ) in the 6–70 μm range.

Throughout this work we adopt the *WMAP* 5 yr cosmological parameters, $H_0 = 70.5$ km s^{-1} Mpc^{-1}, $\Omega_M = 0.27$, $\Omega_\Lambda = 0.73$ (Komatsu et al. 2009). We assume a Kroupa (2001) initial mass function (IMF) for all SFR calibrations. The IR luminosity, $L_{\rm IR}$, of a galaxy refers to the integrated luminosity over the region from 8 to 1000 μm ($L_{\rm IR} = \int_{8\mu{\rm m}}^{1000\mu{\rm m}} L_\nu d\nu$).

2. DATA

2.1. The Spitzer–SDSS–GALEX Spectroscopic Survey (SSGSS) Sample

The SSGSS is a sample of 101 galaxies located within the *Spitzer* Wide-Area Infrared Extragalactic (SWIRE) Survey/Lockman Hole area at $0.03 < z < 0.22$ (Treyer et al. 2010; O'Dowd et al. 2011). These galaxies represent a subset of the 912 galaxies within the Johnson et al. (2006) sample, which has extensive multi-wavelength coverage from *Spitzer*, SDSS, and *GALEX*, and for which *Spitzer* Infrared Spectrograph (IRS) measurements have also been obtained. The UV data are from pipeline-processed *GALEX* observations of these regions with average exposures of $\sim$1.5 ks. The optical photometry comes from the seventh data release of the SDSS main galaxy sample (DR7; Abazajian et al. 2009). The optical spectroscopic measurements are from the Max Planck Institute for Astrophysics and Johns Hopkins University (MPA/JHU) group[5], which is based on the method presented in Tremonti et al. (2004). The IR photometry comes from the SWIRE survey observations (Lonsdale et al. 2003).

Each galaxy in this sample has been observed with the *Spitzer* IRAC and MIPS bands, in addition to observations using the blue filter of the IRS peak-up facility. These blue filter peak-ups have spectral coverage from 13.3–18.7 μm and give an additional photometric point at 16 μm, between the IRAC 8 and MIPS 24 μm bands. Aperture photometry was performed in $7''$ and $12''$ radius apertures for the 3.6–8 μm IRAC and 24 μm MIPS, respectively, and then aperture-corrected to $12.''2$ and $>35''$, respectively. For the MIPS 70 and 160 μm bands, nearly all the galaxies can be treated as point sources, and aperture corrections were taken from the MIPS handbook. A full description of these aperture corrections is described in Johnson et al. (2007). For a more detailed description of the SSGSS dataset, we refer the reader to O'Dowd et al. (2011).

The IRS spectroscopy for the SSGSS sample is obtained through the NASA/IPAC Infrared Science Archive (IRSA) website[6] and is from the work of O'Dowd et al. (2011). This study utilizes the lower resolution Short-Low (SL) and Long-Low (LL) IRS modules, as these have been obtained for the entire SSGSS sample. The SL module spans 5.2–14.5 μm with resolving power $R = 60$–125 and has a slit width of 3.6–$3.''7$. The LL module spans 14–38 μm with resolving power

$R = 57$–126 and has a slit width of 10.5–$10.''7$. The spectra from the two modules were combined by weighted mean and a detailed description of the method can be found in O'Dowd et al. (2011). At $z \sim 0.1$ these galaxies are sufficiently distant such that the IRS slit encompasses a significant fraction of each galaxy (*r*-band Petrosian diameters are $\sim 10''$), providing some of the best MIR SEDs for a continuous SFR(λ) determination.

In order to accurately determine a diagnostic for star formation across the MIR, it is necessary only to consider cases where the majority of light is being contributed from stars (i.e., star-forming galaxies; SFGs) and not from an active galactic nucleus (AGN). The galaxy type is traditionally determined according to its location on the Baldwin–Phillips–Terlevich (BPT) diagram (Baldwin et al. 1981; Kewley et al. 2001; Kauffmann et al. 2003). By adopting the DR7 values of emission line measurements, we find that 64 of the 101 SSGSS galaxies are classified as SFGs. We note that the initial classification of SSGSS galaxies by O'Dowd et al. (2011) utilized SDSS DR4 measurements, which results in a few BPT designations to differ between these works. We further exclude six of the SSGSS galaxies classified as SFGs from our analysis for the following reasons: SSGSS 18 appears to be a merger, SSGSS 19, 22, and 96 have significant breaks in their IRS spectra due to low signal-to-noise ratio (S/N), and SSGSS 35 and 51 suffer from problems with IRS confusion. This leaves 58 galaxies to be used in our calibration of a monochromatic MIR SFR indicator. Table 1 shows the SSGSS IDs of the galaxies used for this study along with some of their properties (additional parameters in the table are introduced in later sections).

Our sample of 58 galaxies spans a redshift range of $0.03 \leqslant z \leqslant 0.22$ with a median redshift of 0.075. The range of IR luminosity is $9.53 \leqslant \log(L_{\rm IR}/L_\odot) \leqslant 11.37$, with a median of 10.55. All measurements of $L_{\rm IR}$ for these galaxies are taken from the original SSGSS dataset (presented in Treyer et al. 2010). The selection criteria for the SSGSS sample was based on 5.8 μm surface brightness and 24 μm flux density, and this restricts our sample of 58 galaxies to relatively high stellar masses $(1.6 \times 10^9 \leqslant M/M_\odot \leqslant 1.7 \times 10^{11})$ and metallicities $(8.7 \leqslant 12 + \log({\rm O/H}) \leqslant 9.2)$. These stellar mass and metallicity estimates are updated from the SSGSS dataset values (based on DR4) to the MPA-JHU DR7 estimates.

2.2. WISE Data

The *WISE* All-Sky Survey provides photometry at 3.4, 4.6, 12, and 22 μm (Wright et al. 2010) which complements the wealth of IR data available for the SSGSS sample. Most importantly for this study, the *WISE* 12 μm band provides a crucial photometric point that bridges the gap between the *Spitzer* 8 and 24 μm bands, a section of the MIR SED that experiences a transition from polycyclic aromatic hydrocarbon (PAH) emission features and dust continuum. The WISE photometry for the SSGSS sample is obtained through the NASA/IPAC Infrared Science Archive (IRSA) website.[7] Using an approach similar to that of Johnson et al. (2007) for the *Spitzer* bands, we utilize the $13.75''$ radius aperture measurements for 12 μm and then apply an aperture correction of 1.20. This correction term was found using sources in our sample with no obvious contamination from neighbors and measuring the flux density out to $24.''75$ to determine their total flux

---

[5]   http://mpa-garching.mpg.de/SDSS/DR7/
[6]   http://irsa.ipac.caltech.edu/data/SPITZER/SSGSS/

[7]   http://irsa.ipac.caltech.edu/Missions/wise.html

Table 1
Summary of Galaxy Properties and IRS Correction Terms

SSGSS ID	R.A. (J2000)	Decl. (J2000)	z	$\log(L_{\mathrm{IR}})$ ($L_\odot$)	$\langle\mathrm{SFR}\rangle$ ($M_\odot\ \mathrm{yr}^{-1}$)	c_{phot}	k	$\frac{(16+k)}{(8+k)}$
1	160.34398	58.89201	0.066	10.55	4.22	0.963	14.10	1.362
2	159.86748	58.79165	0.045	9.83	0.65	1.062	23.64	1.253
3	162.41000	59.58426	0.117	10.59	3.41	1.091	54.09	1.129
4	162.54131	59.50806	0.066	10.22	1.29	0.871	−4.466	3.264
5	162.36443	59.54812	0.217	11.37	19.55	1.088	24.48	1.246
6	162.52991	59.54828	0.115	10.99	7.41	0.851	1.310	1.859
8	161.48123	59.15443	0.044	9.97	0.79	0.843	−5.224	3.882
14	161.92709	56.31395	0.153	11.06	9.60	0.918	10.69	1.428
16	162.04231	56.38041	0.072	10.42	2.15	0.943	15.73	1.337
17	161.76901	56.34029	0.047	10.83	5.58	0.922	21.94	1.267
24	163.53931	56.82104	0.046	10.59	3.43	1.077	0.240	1.971
25	158.22482	58.10917	0.073	10.30	1.89	1.061	2.363	1.772
27	159.34668	57.52069	0.072	11.01	7.70	0.950	−0.933	2.132
30	159.73558	57.26361	0.046	10.11	1.06	1.040	63.01	1.113
32	161.48724	57.45520	0.117	10.82	6.30	1.121	278.9	1.028
34	160.30701	57.08246	0.046	9.96	0.79	0.987	46.47	1.147
36	159.98523	57.40522	0.072	10.39	2.01	0.996	−1.629	2.256
38	160.20963	57.39475	0.118	10.92	6.43	0.905	1.989	1.801
39	159.38356	57.38491	0.074	10.14	1.28	0.684	1.615	1.832
41	158.99098	57.41671	0.102	10.34	1.68	0.818	2.159	1.787
42	158.97563	58.31007	0.155	11.03	9.32	1.170	14.84	1.350
46	159.02698	57.78402	0.044	10.02	0.99	0.932	3.183	1.715
47	159.22287	57.91185	0.102	10.68	4.34	1.331	61.86	1.115
48	159.98817	58.65948	0.200	11.24	15.53	0.869	11.59	1.408
49	159.51942	58.04882	0.091	10.49	3.13	1.107	0.495	1.942
52	160.54201	58.66098	0.031	9.53	0.29	1.129	−2.795	2.537
54	160.41264	58.58743	0.115	11.20	11.53	0.901	6.117	1.567
55	160.29353	58.25641	0.121	10.54	2.95	0.865	3.155	1.717
56	160.41617	58.31722	0.072	10.01	0.85	0.886	4.645	1.633
57	160.12233	58.16783	0.073	9.92	0.75	0.689	15.28	1.344
59	159.89861	57.98557	0.075	10.36	2.00	0.928	15.09	1.346
60	160.51027	57.89706	0.116	10.48	2.89	0.910	6.530	1.551
62	160.91280	58.04736	0.133	11.08	9.85	0.978	0.688	1.921
64	161.00317	58.76030	0.073	10.88	5.44	0.913	3.276	1.709
65	161.37666	58.20886	0.118	11.18	11.85	0.965	12.55	1.389
66	161.25533	57.77575	0.113	10.86	6.75	0.937	13.86	1.366
67	161.18829	58.45495	0.031	10.09	1.21	1.581	8.790	1.476
68	163.63458	57.15902	0.068	10.54	3.37	0.975	25.56	1.238
70	163.17673	57.32074	0.090	10.49	2.81	1.037	255.8	1.030
71	163.21991	57.13160	0.163	10.98	8.32	1.271	285.0	1.027
72	163.25565	57.09528	0.080	10.79	5.01	0.951	14.00	1.364
74	161.95050	57.57723	0.118	10.80	5.07	0.878	−2.430	2.436
76	162.02142	57.81512	0.074	10.55	2.62	0.938	6.128	1.566
77	162.10524	57.66665	0.044	9.69	0.62	1.130	66.79	1.107
78	162.12204	57.89890	0.074	10.56	3.17	1.027	−4.810	3.508
79	161.25693	57.66116	0.045	9.82	0.81	1.023	−0.238	2.031
80	162.07401	57.40280	0.075	10.35	2.14	0.992	−1.949	2.322
81	162.04674	57.40856	0.075	10.24	1.69	0.909	1.709	1.824
82	161.03609	57.86136	0.121	10.77	4.98	0.854	2.444	1.766
83	160.77402	58.69774	0.119	10.92	6.56	0.919	−3.474	2.768
88	161.38522	58.50156	0.116	10.51	2.54	1.106	42.43	1.159
90	162.64168	59.37266	0.153	11.02	8.66	0.796	8.033	1.499
91	162.53705	58.92866	0.117	10.78	5.31	0.782	−3.869	2.937
92	162.65512	59.09582	0.032	10.18	1.42	0.966	6.675	1.545
94	161.80573	58.17759	0.061	10.13	0.90	0.919	9.281	1.463
95	163.71245	58.39082	0.115	10.82	5.74	0.956	22.68	1.261
98	164.14571	58.79676	0.050	10.59	3.70	0.982	5.797	1.580
99	164.33247	57.95170	0.077	10.82	5.58	0.903	−1.944	2.321

Notes. Columns list the (1) galaxy ID number, (2) redshift, (3) integrated infrared luminosity from 8–1000 μm, (4) average SFR from the diagnostics in Table 2, (5) offset between IRS spectra and global photometry above 16 μm (6) correction parameter for wavelength-dependent aperture loss of IRS spectrum below 16 μm, (7) correction factor of the spectrum at 8 μm due to wavelength-dependent aperture loss.

density. The *WISE* photometry at 22 μm is less accurate than the *Spitzer* 24 μm, owing to it having two orders of magnitude lower sensitivity (Dole et al. 2004; Wright et al. 2010), and is not used for our analysis. In addition, the 22 μm observations suffer from an effective wavelength error, which systematically brightens the photometry of SFGs (Wright et al. 2010; Brown et al. 2014).

3. ANALYSIS

3.1. Anchoring the IRS Spectra to Global Photometry

For this study, we focus on utilizing the *Spitzer* 5.8–24 μm and *WISE* 12 μm photometry to anchor the *Spitzer* IRS 5–40 μm spectroscopy available for the entire sample. The reasoning for this approach is to have spectroscopy that is representative of the global flux density of each galaxy, which is required to create a calibrated continuous, monochromatic SFR(λ) indicator. Offsets between the IRS spectrum and the photometry can occur from differences in data reduction methods, or from the width of the IRS slit being smaller than the size of the galaxy. The former effect results in a uniform offset across the entire spectra and can be corrected with a normalization factor. The behavior of the latter effect will be dependent on whether the galaxy observed is an unresolved point-like source. The default *Spitzer* IRS custom extraction (SPICE) does include a correction for light lost from the slit due to the changing angular resolution as a function of wavelength but assumes the object to be a point source. To correct for both of these effects, we utilize photometry from the *Spitzer* 8, 16, and 24 μm and *WISE* 12 μm bands as a reference. The end-of-channel transmission drop of the SL module below ~5.8 μm, combined with a typical redshift of $z \sim 0.1$, makes the 5.8 μm band region unreliable for use in most cases, and so it is not used as an anchor. However, we do make use of the 5.8 μm band to inspect our photometric matching in the lowest redshift galaxies (see below). Here we outline our approach to correct for offset effects so that these spectra are well representative of global photometric measurements.

O'Dowd et al. (2011) found that IRS measurements of SSGSS galaxies from the LL module did not show evidence for significant aperture loss when compared to the *Spitzer* 16 and 24 μm photometry. This is attributed to the fact that the lower resolution (larger PSF) of sources in this longer wavelength module, coupled with the larger slit width of 10″6 allows for the standard SPICE algorithm to accurately recover the total flux density, since objects are close to point sources (see O'Dowd et al. 2011). This would suggest that any offsets between the photometry and spectroscopy beyond 16 μm should be uniform across the module (i.e., a global loss in flux density). Therefore, each spectrum is first fit to match the 16 and 24 μm photometric points using a constant offset, c_{phot}, found using chi-squared minimization,

$$c_{\mathrm{phot}} = \frac{\sum_i \left(S_{\mathrm{phot},i} S_{\mathrm{IRS},i} \right) \big/ \sigma \left(S_{\mathrm{phot},i} \right)^2}{\sum_i \left(S_{\mathrm{phot},i} \big/ \sigma \left(S_{\mathrm{phot},i} \right) \right)^2} \quad (1)$$

$$\chi^2 = \sum_i \left(\frac{S_{\mathrm{phot},i} - c_{\mathrm{phot}} S_{\mathrm{IRS},i}}{\sigma \left(S_{\mathrm{phot},i} \right)} \right)^2, \quad (2)$$

where $S_{\mathrm{phot},i}$ is the *Spitzer* photometric flux density of band i, σ ($S_{\mathrm{phot},i}$) is the uncertainty of the *Spitzer* photometric flux

density, and $S_{\mathrm{IRS},\,i}$ is the effective IRS photometric flux density found using the transmission curve for each band, $T_i(\lambda)$,

$$S_{\mathrm{IRS},i} = \frac{\int S_{\mathrm{IRS}}(\lambda) T_i(\lambda) d\lambda}{\int T_i(\lambda) d\lambda}. \quad (3)$$

This method ignores the method of calibration that was utilized for each specific bandpass (i.e., a conversion of number of electrons measured by the detector into a flux density in Jy requires knowing the shape of the incoming flux of an object, which varies as a function of wavelength). However, discrepancies between the adopted method and correcting for calibration effects amount to ~1%, and is not important for this study. The offset required to match photometric values is typically small, with values of c_{phot} being between 0.7–1.6.

In contrast to the LL module, O'Dowd et al. (2011) found that IRS measurements short-ward of 16 μm from the SL module did show evidence for aperture loss when compared to the *Spitzer* 8 μm photometry. In this case, the increasing resolution of the SL module at shorter wavelengths results in many of the galaxies in this sample being resolved in this module. Also taking into account that the SL slit is 3″6, which is smaller than the average extent of ~10″ (*r*-band Petrosian diameter) for SSGSS galaxies, implies that flux density loss in this wavelength region is more pronounced for more extended objects. For this reason, an additional correction term must be introduced below 16 μm which has a 1/λ dependency to reflect the additional losses as resolution increases at shorter wavelengths (i.e., the PSF is decreasing at shorter wavelengths, resulting in less correction of light outside the slit). The correction terms adopted are summarized in the following equations,

$$S_{\mathrm{IRS,corr}}(\lambda) = \begin{cases} S_{\mathrm{IRS}}(\lambda)/c_{\mathrm{phot}} \times \left(\dfrac{16 + k}{\lambda + k} \right) & : \lambda < 16\,\mu\mathrm{m}, \\ S_{\mathrm{IRS}}(\lambda)/c_{\mathrm{phot}} & : \lambda \geqslant 16\,\mu\mathrm{m} \end{cases} \quad (4)$$

where k is a constant found by performing a Levenberg–Marquardt least-squares fit of this function, using the IDL code MPFITFUN (Markwardt 2009), such that the IRS spectrum matches the 8 and 12 μm photometric flux density. Smaller values of k correspond to larger correction factors in the spectrum. Examples of normalizing the IRS spectroscopy to the photometry are shown in Figure 1. A list of the normalization parameters is shown in Table 1.

As a consistency check on the 1/λ dependency, a more accurate check is made on the few cases where spectra have high S/N and low redshifts, such that the 5.8 μm band region of the spectrum is reliable to use for convolution. In nearly all these cases the correction using a 1/λ dependency matches the observed photometric point, as demonstrated by SSGSS 46 in Figure 1. In addition, the agreement of the *Spitzer* 8 μm and *WISE* 12 μm data with this approach suggests these normalized spectra are well representative of photometric values.

3.2. Extending Out to 70 μm

The IRS spectrum extends out to 40 μm; however, the combination of end-of-channel transmission drop around $\lambda_{\mathrm{obs}} \sim 37\,\mu$m and redshift effects makes these spectra unreliable for $\lambda_{\mathrm{rest}} \gtrsim 37/(1+z)\,\mu$m. For the mean redshift of this sample ($z \sim 0.1$), this corresponds to roughly $\lambda_{\mathrm{rest}} \sim 34\,\mu$m. In order to utilize the wavelength region between 34 and 70 μm,
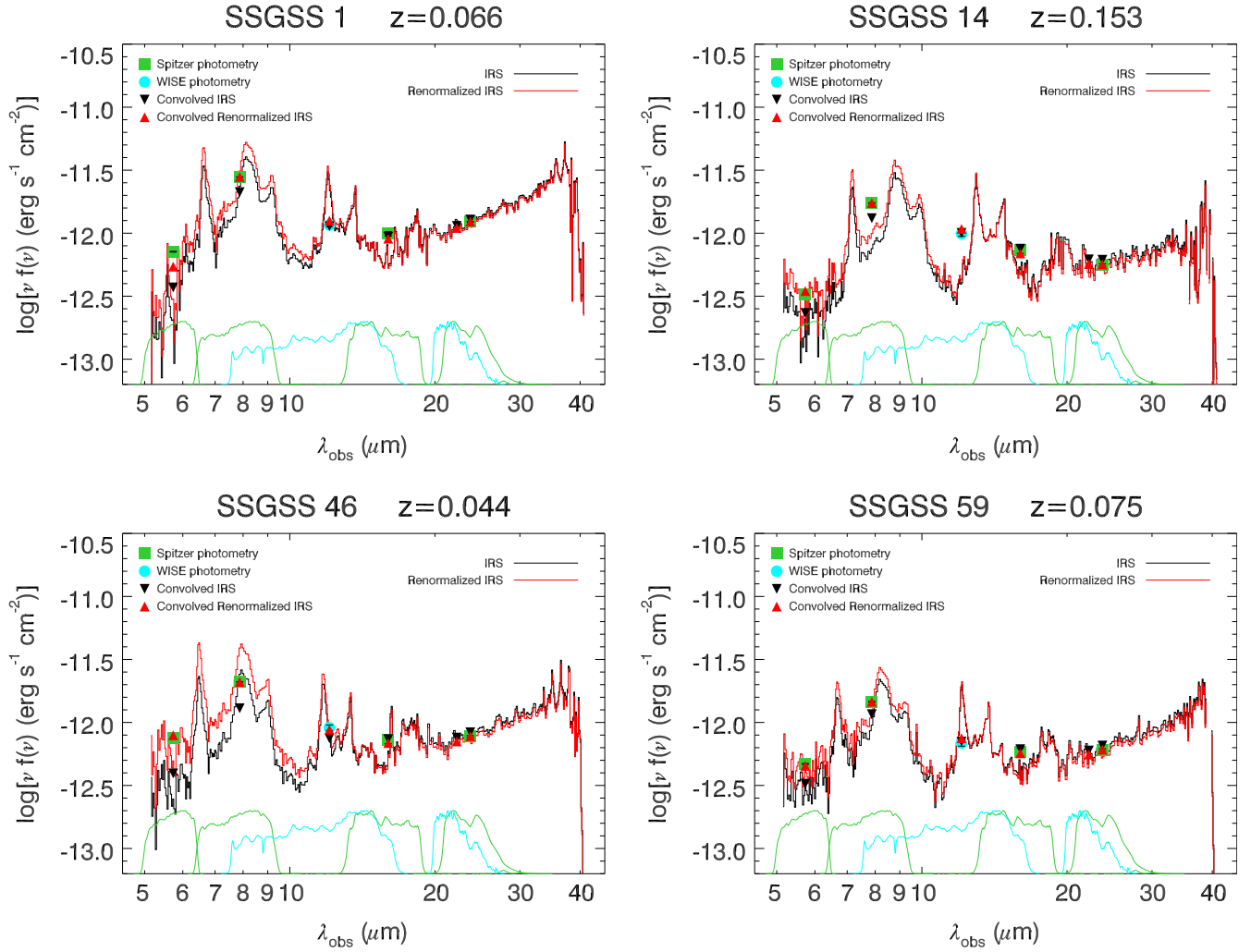
Figure 1. IRS spectroscopy (black line), *Spitzer* photometry (green squares), and *WISE* photometry (cyan circle) for some SSGSS galaxies. The IRS spectrum is normalized to the *Spitzer* 8, 16, and 24 μm and *WISE* 12 μm photometric flux densities according to the method described in Section 3.1 (red line). The effective IRS photometry, found using the transmission curve for each bandpass filter, is shown as triangles. The normalized transmission curves for the *Spitzer* and *WISE* bands in this region are shown as green and cyan lines, respectively.

which contains poor quality or no spectral data, we interpolate with dust models. This interpolation is expected to be robust since there are no sharp emission features in this wavelength range. The shape of the emission in this region is dependent on the temperature distribution of of the dust, the grain size distribution, as well as the relative importance of stochastic versus thermal equilibrium heating (the former gives an almost-constant continuum and the latter is responsible to the Wien-like rise of the spectrum).

To extend the wavelength region of our study out to 70 μm, we fit the dust models of Draine & Li (2007), combined with an additional stellar continuum component, to our IR photometry and IRS spectroscopy. For these models, the emission spectrum is given by Draine et al. (2007) as

$$S_{\nu,\text{model}} = \Omega_* B_\nu(T_*) + \frac{M_{\text{dust}}}{4\pi D_{\text{lum}}^2}\Big[(1-\gamma)p_\nu^{(0)}(j_M, U_{\text{min}})$$
$$+ \gamma p_\nu(j_M, U_{\text{min}}, U_{\text{max}}, \alpha)\Big], \qquad (5)$$

where Ω_* is the solid angle subtended by stars, T_* is the effective temperature of the stellar contribution, M_{dust} is the total dust mass, D_{lum} is the distance to the galaxy, p_ν is the

specific power per unit dust mass, U_{min} (U_{max}) is the minimum (maximum) interstellar radiation, γ is the fraction of the dust mass exposed to radiation with intensity $U > U_{\text{min}}$, j_M corresponds to the dust model (i.e., the PAH abundance relative to dust, q_{PAH}; shown in Table 3 of Draine & Li 2007), and α is the power-law factor for the starlight intensity. In summary, this emission spectrum is a linear combination of three components: (1) a stellar continuum with effective temperature T_* which dominates at $\lambda \lesssim 5\,\mu$m; (2) a diffuse ISM component with an intensity factor $U = U_{\text{min}}$; and (3) a component arising from photo-dissociation regions. Typically, component (2) comprises a much larger amount of the total dust mass and, as such, is dominant over component (3) in the emission spectrum (Draine et al. 2007, 2014).

To fit this model we follow the approach outlined in Draine et al. (2007), which found that the SEDs of galaxies in the *Spitzer* Infrared Nearby Galaxies Survey (SINGS) were well reproduced with fixed values of $\alpha = 2$, $U_{\text{max}} = 10^6$, and $T_* = 5000$ K. Holding these parameters fixed, q_{PAH}, U_{min}, γ, M_{dust}, and Ω_* are varied to find the dust model that comes closest to reproducing the photometry and spectroscopy. For this work, a grid of γ values is constructed for all q_{PAH} (MW,
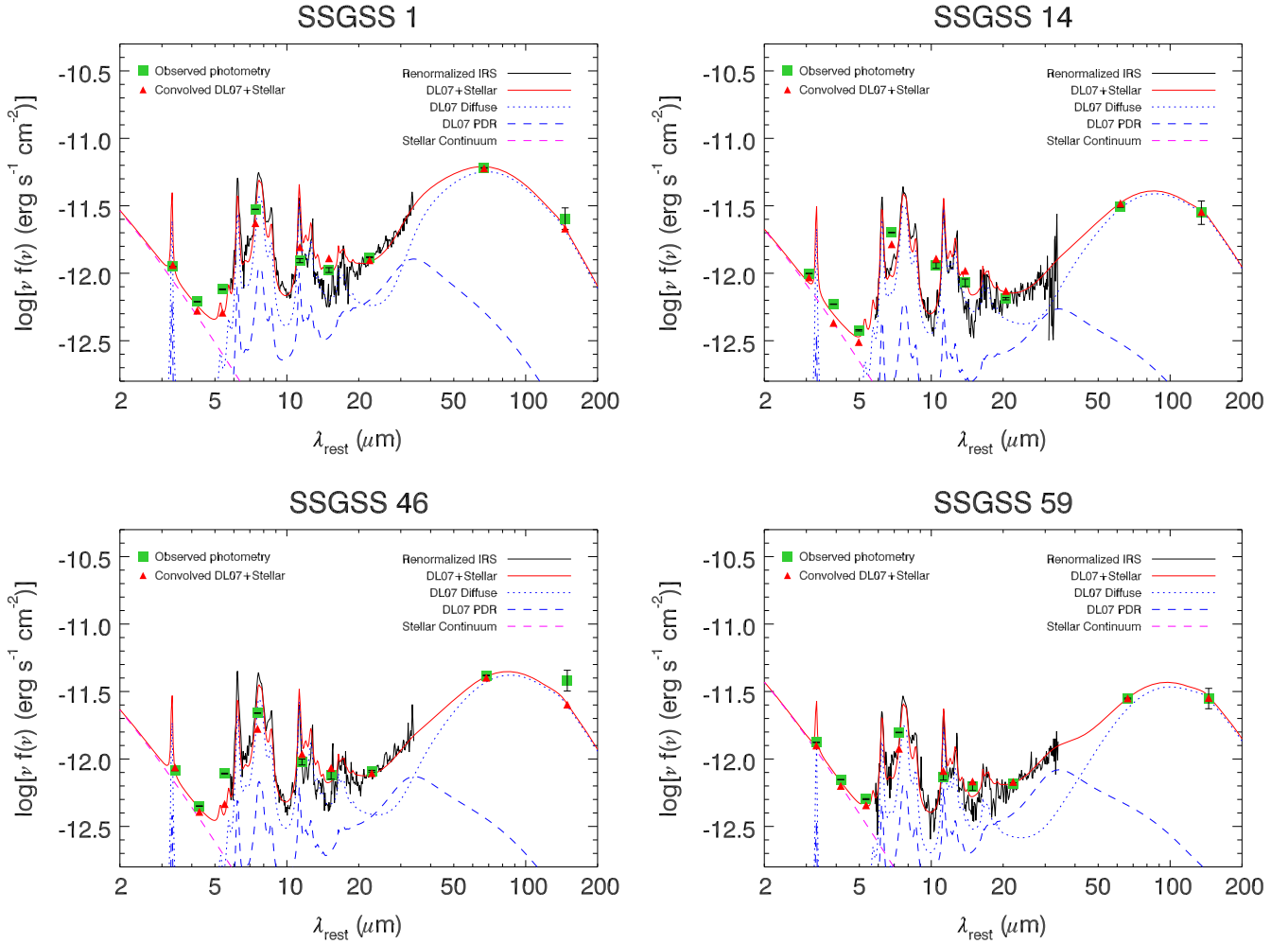
Figure 2. A fit to the spectra of some SSGSS galaxies using the dust models of Draine & Li (2007), shown as the solid red line. The IRAC 3.6, 4.5, and 5.8 μm along with the MIPS 70 and 160 μm photometry is used to fit the dust continuum in the absence of the IRS spectrum. The bands within the IRS region are shown for comparison and not used directly for the fit. The regions of the IRS spectrum associated with transmission drops in the instrument are not shown for clarity. We attribute the relatively poor match in the 6–20 μm region to using a simple three-component model. However, the purpose of these fits is only to determine the shape of emission in the 34–70 μm region, for which the data is found to be in good agreement with the models.

LMC, SMC) and U_{min} values. The value of M_{dust} for each grid point is determined by minimizing the χ^2 parameter in a similar manner to Equations (1) and (2), as M_{dust} represents a constant offset value. The goodness-of-fit for each case is assessed using the χ^2 parameter,

$$\chi^2 \equiv \sum_i \frac{S_{obs,i} - S_{model,i}}{\sigma^2_{obs,i} + \sigma^2_{model,i}}, \qquad (6)$$

where the sum is over observed bands and spectroscopic channels, $S_{model,i}$ is the model spectrum (for band comparison, the model spectrum is convolved with the response function of that band), $\sigma_{obs,i}$ is the observational uncertainty in the observed flux density $S_{obs,i}$, and $\sigma_{model,i} = 0.1 S_{model,i}$ as adopted by Draine et al. (2007). The observed flux densities used in determining the best fit is comprised of the IRS spectroscopy in addition to the IRAC 3.6, 4.5, and 5.8 μm and MIPS 70, and 160 μm photometry. The model which minimizes the value of χ^2 is adopted for use in representing the region $\lambda_{rest} \gtrsim 37/(1+z)$ μm. Examples of the best fitting model for SSGSS galaxies are shown in Figure 2. The bands within the IRS region are shown only for comparison and are not used directly for the fit.

Our choice to adopt the model which minimizes the value of χ^2 is not necessarily the most accurate representation of the spectra, as the degeneracy of the model parameters can allow for multiple fits to have similar χ^2 values while having different FIR SED shapes. However, we do not consider this to be of great significance for this study for two reasons. First, the flux density variation due to changes in the SED shape for cases with $(\bar{\chi}^2 - \bar{\chi}^2_{min}) < 1$, where $\bar{\chi}^2_{min}$ is the minimum value of the reduced χ^2, is typically less than 25% over the 30–70 μm region, which is lower than the scatter among individual galaxy templates. As we will be utilizing an average of our galaxy templates for our diagnostic, the uncertainty from model SED variations will not be the dominant source of uncertainty. Second, the parameters of these fits are not used to determine the properties of these galaxies, which are more sensitive to these degeneracy effects than the total flux density.

All cases are best fit by Milky Way dust models with $q_{PAH} \geqslant 2.50\%$. There is a systematic trend among most fits to underestimate the flux density around the 8 μm PAH feature and overestimate the 10–20 μm region. This is most likely due to the limitations of fitting only three components to the data. However, since the main focus of these fits is to provide a

Table 2
Reference Star Formation Rate Calibrations

Band(s)	L_x Range (erg s^{-1})	SFR	$\log C_x$	Reference
FUV+TIR	⋯	$[L(\mathrm{FUV})_{\mathrm{obs}} + 0.46\, L(\mathrm{TIR})]/C_x$	43.35	Hao et al. (2011)
FUV+24 μm	⋯	$[L(\mathrm{FUV})_{\mathrm{obs}} + 3.89\, L(24)]/C_x$	43.35	Hao et al. (2011)
NUV+TIR	⋯	$[L(\mathrm{NUV})_{\mathrm{obs}} + 0.27\, L(\mathrm{TIR})]/C_x$	43.17	Hao et al. (2011)
NUV+24 μm	⋯	$[L(\mathrm{NUV})_{\mathrm{obs}} + 2.26\, L(24)]/C_x$	43.17	Hao et al. (2011)
Hα+8 μm	⋯	$[L(\mathrm{H}\alpha)_{\mathrm{obs}} + 0.011\, L(8)]/C_x$	41.27	Kennicutt et al. (2009); Hao et al. (2011)
Hα+24 μm	⋯	$[L(\mathrm{H}\alpha)_{\mathrm{obs}} + 0.020\, L(24)]/C_x$	41.27	Kennicutt et al. (2009); Hao et al. (2011)
Hα+24 μm	$L(24) < 4 \times 10^{42}$	$[L(\mathrm{H}\alpha)_{\mathrm{obs}} + 0.020\, L(24)]/C_x$	41.26	Calzetti et al. (2010)
	$4 \times 10^{42} \leqslant L(24) < 5 \times 10^{43}$	$[L(\mathrm{H}\alpha)_{\mathrm{obs}} + 0.031\, L(24)]/C_x$	41.26	Calzetti et al. (2010)
	$L(24) \geqslant 5 \times 10^{43}$	$L(24) \times [2.03 \times 10^{-44} L(24)]^{0.048}/C_x$	42.77	Calzetti et al. (2010)
Hα+TIR	⋯	$[L(\mathrm{H}\alpha)_{\mathrm{obs}} + 0.0024\, L(\mathrm{TIR})]/C_x$	41.27	Kennicutt et al. (2009); Hao et al. (2011)
24 μm	$2.3 \times 10^{42} \leqslant L(24) \leqslant 5 \times 10^{43}$	$L(24)/C_x$	42.69	Rieke et al. (2009)
	$L(24) > 5 \times 10^{43}$	$L(24) \times (2.03 \times 10^{-44} L(24))^{0.048}/C_x$	42.69	Rieke et al. (2009)
70 μm	$L(70) \gtrsim 1.4 \times 10^{42}$	$L(70)/C_x$	43.23	Calzetti et al. (2010)

Notes. Columns list the (1) bands used in the calibration, (2) luminosity range over which the calibration can be used; empty fields denote an unspecified range, (3) SFR conversion formula, (4) conversion constant, and (5) reference for calibration.

description of the region from ∼34–70 μm, these deviations are not considered to be significant, as they should have little effect on matching the shape of the emission beyond ∼34 μm. As will be discussed in Section 6.2, these fits are consistent with other $z = 0$ SFG templates found in the literature that make use of Draine & Li (2007) models, suggesting that these deviations could be a common problem. Investigation into the cause of these discrepancies warrants additional study, as it will improve our understanding of dust properties in galaxies. We do not make use of these fits to determine L_{IR} values, instead using the values provided in the SSGSS catalog, which have been extensively checked (Treyer et al. 2010) across a variety of diagnostic methods.

3.3. Determining Rest-frame Luminosities

As these galaxies span a redshift range of $0.03 \leqslant z \leqslant 0.22$, the IRS spectrum and photometry of each galaxy span slightly different regions in rest-frame wavelength. This offset causes observed photometric values to vary by up to 30% from the rest-frame values. This would affect our determination of SFR if not accounted for and introduce additional scatter. Since previous MIR calibrations have been performed for local samples of galaxies ($z \sim 0$) to accuracies around 30% (Rieke et al. 2009; Kennicutt et al. 2009; Calzetti et al. 2010; Hao et al. 2011), this is a non-negligible effect.

To correct for redshift effects, photometric values for each band are determined by convolving the spectrum at the rest-frame filter postions for each band according to Equation (3), only now using the corrected spectrum, $S_{\mathrm{IRS,corr}}(\lambda)$, instead of the original IRS spectrum. This is performed for the *Spitzer* 8, 24, and 70 μm and *WISE* 12 and 22 μm bands. These corrected flux densities are used to calculate the rest-frame luminosity (erg s^{-1}) of each band,

$$L_{\mathrm{rest}} = \left(\nu L_\nu\right)_{\mathrm{rest}} = \left(\nu S_{\mathrm{IRS,corr}}\right)_{\mathrm{obs}} 4\pi D_{\mathrm{lum}}^2, \qquad (7)$$

where ν_{rest} and ν_{obs} are the effective rest-frame and observer-frame frequency of each band, respectively, and D_{lum} is the luminosity distance for the galaxy, calculated from its redshift. These rest-frame luminosities are used to determine SFRs for each of the galaxies in our sample. In a similar manner, each

IRS spectrum is expressed as a wavelength dependent rest-frame luminosity, $L(\lambda)_{\mathrm{rest}}$, using the continuous spectrum, $S_{\mathrm{IRS,corr}}(\lambda)$. This is used later for calibrating our wavelength continuous SFR-luminosity conversion factors, $C(\lambda)$.

To correct the *Spitzer* 3.6 and 4.5 μm bands, which lie outside of the IRS spectral coverage, a correction is applied assuming these bands encompass the Rayleigh–Jeans tail of the stellar continuum emission,

$$S'_{\mathrm{obs}} = S_{\mathrm{obs}} \left(\frac{\lambda_{\mathrm{rest}}}{\lambda_{\mathrm{obs}}}\right)^{-2} = S_{\mathrm{obs}} \times (1+z)^{-2}. \qquad (8)$$

The luminosity is then found following Equation (7) using S'_{obs}. The rest-frame *Spitzer* 3.6 and 4.5 μm luminosities will only be used to examine the origins of scatter within our conversion factors in Section 6.1, and has no influence on our estimates for the MIR conversion factors. The fitting results in Section 3.2 suggest that this simple approach is reasonable for our sample of SFGs.

3.4. Reference Monochromatic SFR Indicators

In order to perform any calibration of luminosity as a SFR indicator, it is necessary to rely on previous, well-calibrated SFR indicators. In this work, we utilize the calibrations of Kennicutt et al. (2009), Rieke et al. (2009), Calzetti et al. (2010), and Hao et al. (2011), which incorporate the full suite of data available for this sample. This list is shown in Table 2. The reference SFR, ⟨SFR⟩, for each galaxy is taken to be the average of the SFRs from these calibrations. By utilizing the average of a large number of diagnostics, we limit the risk of potential biases that any single diagnostic can be subject to. Several of these reference diagnostics make use of the total IR luminosity, L_{TIR}, which refers to the integrated luminosity over the region from 3 to 1100 μm. All measurements of L_{TIR} for these galaxies have been obtained from the original SSGSS dataset (Treyer et al. 2010). For the SSGSS sample, Treyer et al. (2010) find that L_{TIR} is larger than L_{IR} by ∼0.04 dex.

To utilize SDSS measurements of Hα for a SFR estimation, it is necessary to apply an aperture correction. The diameter of the SDSS spectroscopic fiber spans 3″, which is a factor of ∼3 smaller than the typical size of the SSGSS galaxies and results
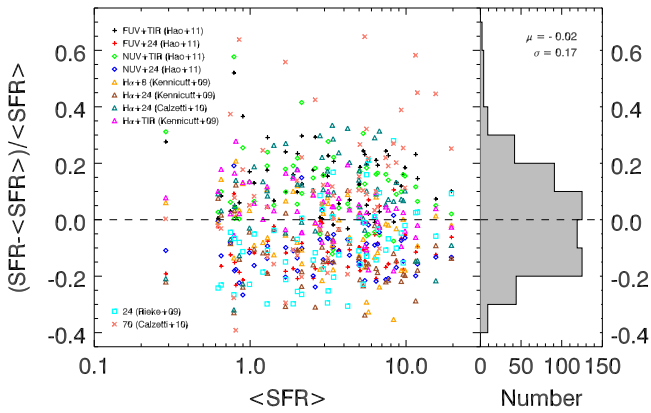
Figure 3. Left: comparison of SFRs determined from the calibrations listed in Table 2 for the SFGs in the SSGSS. Each vertical strip of values shows the SFR values for each method on a single galaxy. The reference SFR, ⟨SFR⟩, for these galaxies is taken to be the average of the SFR values from these calibrations. Right: histogram showing the distribution of SFR offsets relative to the reference value. This distribution is well fit by a Gaussian with $\mu = -0.02$ and $\sigma = 0.17$, suggesting that the majority of these values agree within the uncertainties associated with the individual calibrations.

in only a fraction of the light being measured. We correct for this aperture effect using the prescription from Hopkins et al. (2003), which uses the difference between the r-band Petrosian magnitude and the r-band fiber magnitude (see also Treyer et al. 2010). The values of these corrections range from 1.9–8.3 for our sample, with the exception of SSGSS 67 with a correction of 21.4 due to its much larger size.

As a consistency check, the SFRs inferred from each indicator for our galaxies are compared in Figure 3. It is seen from the distribution that the majority of these values agree within the ~30% uncertainty associated with individual calibrations (Rieke et al. 2009; Kennicutt et al. 2009; Calzetti et al. 2010; Hao et al. 2011). A formal fit of this distribution to a Gaussian profile gives values of $\mu = -0.02$ and $\sigma = 0.17$. Our choice in using the average of the diagnostics, ⟨SFR⟩, for each galaxy instead of the median value appears to cause no significant differences, with typical offsets of only a few percent between the two, which are symmetric. A formal Gaussian fit of fractional difference between the mean and median gives $\mu = -0.01$ and $\sigma = 0.04$. We illustrate the relative offsets for the individual calibrations in Figure 4. We note that the MPA/JHU group provides independent estimates for SFRs based on the technique discussed in Brinchmann et al. (2004) using extrapolated Hα measurements. However, we find that the spread in values for these estimates relative to ⟨SFR⟩ are significantly larger than our other diagnostics ($1\sigma = 0.48$), which we attribute to their larger SFR uncertainties (~50%), and as such were excluded from our analysis (including Figures 3 and 4).

3.5. L_{IR} as an SFR Indicator

A commonly utilized method to determine SFRs for galaxies relies on measuring the integrated luminosity over most of the IR wavelength range, L_{IR} (8–1000 μm). However, physically understanding the conversion of L_{IR} to a SFR is non-trivial and sensitive to many assumptions, such as the timescale of star formation, τ, the star formation history (SFH), the metallicity, and the initial mass function (IMF; see Murphy et al. 2011b; Calzetti 2013). For example, a galaxy with a constant SFH, a fixed metallicity, and a fixed IMF will have the calibration

constant for L_{IR} change by a factor of 1.75 between assuming $\tau = 100$ Myr and $\tau = 10$ Gyr (Calzetti 2013).

We chose to avoid the use of SFRs based solely on L_{IR} for reference because of the sensitivity to these assumptions. However, in order to compare the accuracy of our calibration on higher redshift samples (in Section 6.4) for which L_{IR} is the only technique available to estimate SFRs, we use a SFR-L_{IR} conversion which reproduces the values of ⟨SFR⟩ seen for the SSGSS sample. This occurs for a conversion factor of $\log[C(L_{IR})] = 43.64$ erg s^{-1} ($M_\odot$ yr^{-1}). Utilizing Starburst (SB) 99 (Leitherer et al. 1999), with a constant SFH, solar metallicity, a Kroupa IMF over 0.1–100 $M_\odot$, and assuming all of the stellar light (UV+visible) is reradiated by dust, this corresponds to a timescale of $\tau \sim 500$ Myr (e.g., Calzetti 2013).

This adopted conversion factor differs slightly from other commonly adopted values. In the case of Murphy et al. (2011b), $\log[C(L_{IR})] = 43.41$ erg s^{-1} ($M_\odot$ yr^{-1})$^{-1}$, our calibration is larger by 70%. This large difference is due to two reasons: (1) Murphy et al. (2011b) assume that only UV light is being reradiated by the dust and does not account for the optical light that would also be reradited (~40% of the discrepancy), and (2) they assume a 100 Myr constant star-forming population (~20% of the discrepancy). In the case of Kennicutt (1998) after converting from a Salpeter (1955) IMF to a Kroupa (2001) IMF, $\log[C(L_{IR})] = 43.53$ erg s^{-1} ($M_\odot$ yr^{-1})$^{-1}$, our calibration is larger by 30%. Most of this difference is due to them assuming a 100 Myr constant star-forming population.

4. A CALIBRATED CONTINUOUS, MONOCHROMATIC SFR(λ)

4.1. Composite IRS Spectrum

The SFR of a galaxy, using a calibrated single-band luminosity, can be written as

$$\text{SFR}\left(M_\odot \text{yr}^{-1}\right) = L_x/C_x, \qquad (9)$$

where L_x is the monochromatic luminosity, in units of erg s^{-1}, and C_x is the conversion factor between SFR and luminosity for filter x (following convention of Kennicutt & Evans 2012). In this respect, the appropriate conversion factor at a given band is found by normalizing the luminosity by the SFR determined independently from a reference calibration.

This same approach is taken to calibrate our continuous wavelength conversion factors,

$$C(\lambda)\left(\text{erg s}^{-1}\left(M_\odot \text{yr}^{-1}\right)^{-1}\right) = L(\lambda)_{\text{rest}}/\langle\text{SFR}\rangle, \qquad (10)$$

where $L(\lambda)_{\text{rest}}$ is the wavelength dependent IRS luminosity and ⟨SFR⟩ is the reference SFR. To achieve our calibration of $C(\lambda)$, the SFR-normalized IRS spectra are averaged together to create a composite spectrum for the group. As a result of shifting the spectra to the rest-frame, the wavelengths associated with each spectral channel no longer match exactly. Therefore, to perform this average, the channel wavelengths in the spectrum of the first galaxy in our group is taken to be the reference grid. Next, the normalized luminosity values of the other galaxies are re-gridded to this (i.e., each channel is associated to the nearest neighboring reference channel). In using this approach, the smoothing of sharp features that result from direct interpolation is avoided. The uncertainties associated with this re-gridding to determine a composite spectrum are small relative to the channel flux density uncertainly. Furthermore, these
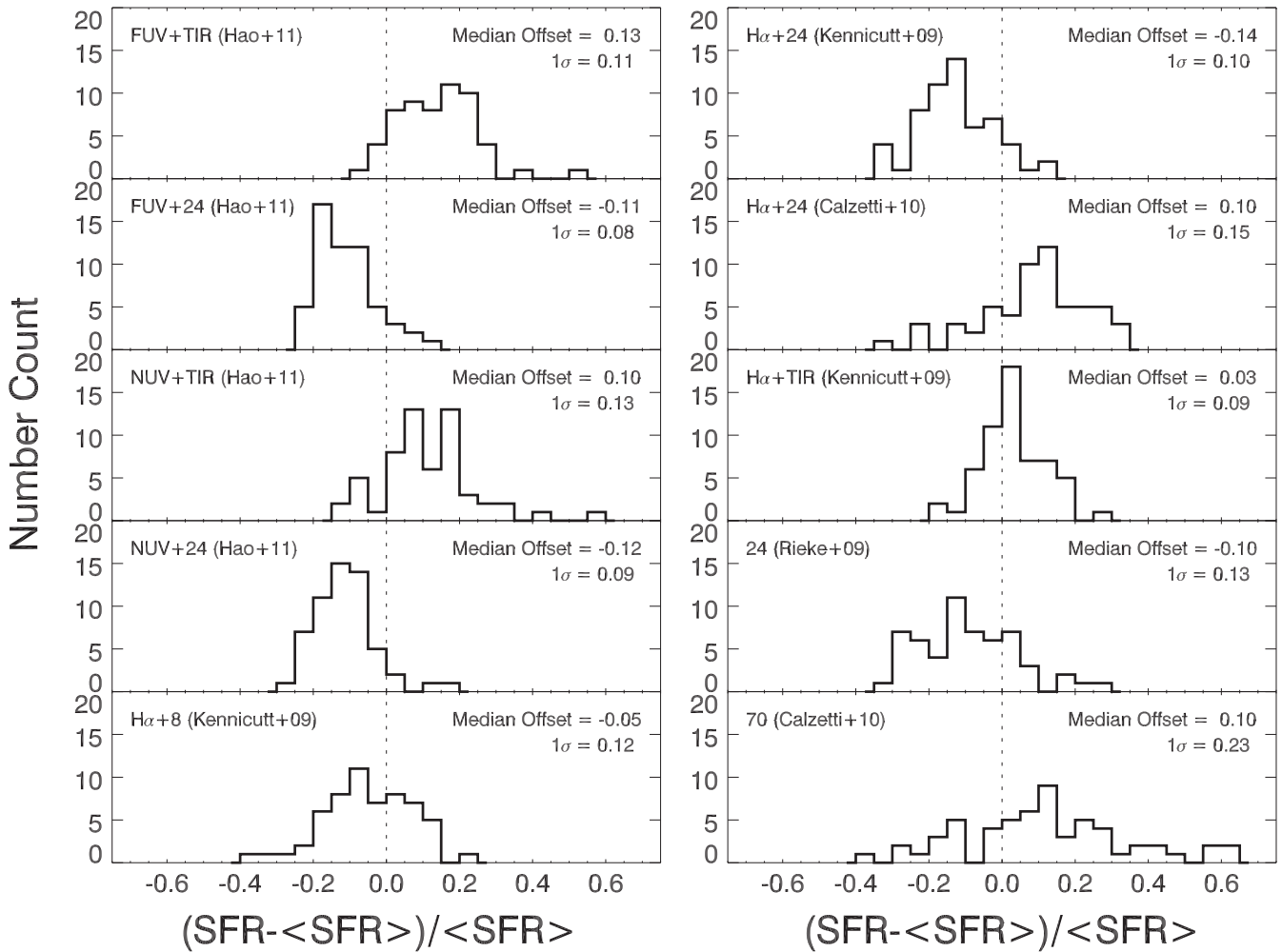
Figure 4. Histograms showing the distribution of the individual SFR estimates relative to the reference value, ⟨SFR⟩. The calibrations being considered are listed in Table 2. The median offset and 1σ dispersion are shown in each panel.

uncertainties are much smaller than the scatter between spectra, which drives the uncertainty of our template, and can be considered negligible for the purposes of this study.

The result of an average for the entire sample of SFGs in the SSGSS sample is shown in Figure 5. The uncertainty of each channel in the composite spectrum is taken to be the standard deviation of the the group value for that channel. The sample standard deviation is the dominant source of uncertainty (typically between 20–30% of the normalized luminosity value) and is larger than the flux density uncertainties of individual IRS channels (typically ~2%) by roughly an order of magnitude. This template can be used to determine the appropriate conversion factor for any luminosity within our wavelength coverage.

4.2. Filter Smoothed Composite Spectrum

In practice, observations of a galaxy are made using specific bandpass filters that encompass a portion of their SED. Therefore, it is more practical to utilize a composite spectrum that corresponds to photometric luminosities observed by various bands as functions of redshift. To accomplish this, the normalized IRS spectrum of each SFG in our sample is convolved with the filter response of specific bands as

functions of redshift (i.e., the effective wavelength blue-shifts and the bandpass narrows, both by a factor of $(1 + z)$, as one goes to higher redshifts). Performing this convolution is similar to smoothing by the bandpass filter, only with the filter width changing with redshift. Throughout the rest of this paper, the term "smoothed" is used interchangeably to mean this convolution process. The redshift limit imposed for each band occurs at the shortest usable rest-frame wavelengths of the IRS spectrum for that band. The composite IRS template and the filter smoothed composites presented in this Section are publicly available for download from the IRSA.[8]

Each normalized IRS spectra is smoothed using the *Spitzer*[9,10], *WISE*[11], and *JWST*/MIRI filters. The properties of these filters is listed in Table 3. We note that the *Herschel* PACS 70 μm is close enough to *Spitzer* 70 μm that these can be interchanged for use with $C_{S70}(\lambda)$. We emphasize to the reader that care should be taken when considering the 22 μm band, as it has been shown to suffer from an effective wavelength error

---

[8]　http://irsa.ipac.caltech.edu/data/SPITZER/MIR_SFR
[9]　http://irsa.ipac.caltech.edu/data/SPITZER/docs/irac/iracinstrumenthandbook/
[10]　http://irsa.ipac.caltech.edu/data/SPITZER/docs/mips/mipsinstrumenthandbook/
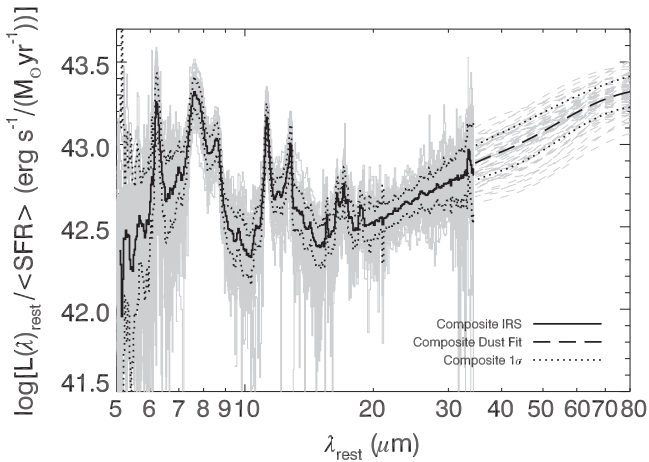[11]　http://astro.ucla.edu/~wright/WISE/passbands.html

Figure 5. Normalized IRS luminosity, $L(\lambda)_{\rm rest}/\langle {\rm SFR} \rangle$, for all SFG galaxies (gray solid lines). The composite spectrum of this group is shown (thick black line) along with the standard deviation from this average (black dotted lines), which at most wavelengths is between 20 and 30%. The fits to the dust continuum for each galaxy (gray dashed lines; described in Section 3.2) along with the average (black dashed line) are also shown. The low dispersion among normalized spectra suggests that the 6–70 μm region can be utilized for SFR diagnostics.

(see Wright et al. 2010; Brown et al. 2014). For the MIRI filters, we use the response functions of Glasse et al. (2015). Since these curves do not take into account the wavelength dependent quantum efficiency, the instrument transmission, or the responsivity of the detector, they should be updated once better curves become available.

The composite spectra for each of these bands is created by averaging the smoothed spectra together, in the same manner as for the group average. The result of averaging the convolved spectra is shown in Figures 6 and 7. The associated uncertainty with each channel (sample standard deviation) is slightly lower than the native composite spectrum owing to the smoothing from the convolution and is typically between 15 and 20% of the normalized luminosity value (except for 70 μm case, which is still around 30%), making them comparable to accuracies achieved in many previous calibrations. Previously determined MIR conversion factors (from $z \sim 0$ samples) are also shown and appear in good agreement.

For the filter bands considered here, the smoothed IRS spectra show a very large increase in scatter below $\sim 6\,\mu$m, which is due to a combination of the end-of-channel uncertainties being very high and also from variations in the old stellar populations of these galaxies. For these reasons, we only consider the regions for which the 1σ uncertainty is less than 30% suitable for calibration. In the case of the WISE 12 μm band, this region occurs below $\sim 7\,\mu$m because of the significantly wider filter bandwidth. The ranges chosen for the calibration of each band is shown in Table 4.

4.3. Fits to the Composite Spectra

To simplify the application of our results as SFR indicators, each of the filter smoothed composite spectra is fit using a continuous function, $\mathrm{fit}_x(\lambda)$. We perform Levenberg–Marquardt least-squares fits of a polynomial (up to first order) and Drude profiles (up to five), $I_r(\lambda)$, to the smoothed composite

spectra, using the IDL code MPFITFUN,

$$\mathrm{fit}_x(\lambda) = \sum_{i=1}^{2} p_i \lambda^{(i-1)} + \sum_{r=1}^{5} I_r(\lambda), \tag{11}$$

where x corresponds to the filter being considered, p_i are constants, and $I_r(\lambda)$ are Drude profiles, which are typically employed to characterize dust features, and have the form

$$I_r(\lambda) = \frac{b_r \gamma_r^2}{\left(\lambda/\lambda_r - \lambda_r/\lambda\right)^2 + \gamma_r^2}, \tag{12}$$

where λ_r is the central wavelength of the feature, γ_r is the fractional FWHM, and b_r is the central intensity, which is required to be non-negative. We emphasize that because these are smoothed spectra, the parameters of these fits are not of physical significance and are simply being employed for ease of application.

For the Drude profiles, the central wavelengths, λ_r, are fixed to wavelengths that roughly correspond to the peaks in the smoothed spectrum, while γ_r and b_r are left as free parameters. Therefore, there are up to 12 free parameters in total, two from the polynomial and ten from the Drude profiles. The values of λ_r for each smoothed composite fit and all the other fit parameters are listed in Table 4. The fits are shown for the individual bands in Figure 6. The fitting functions are typically accurate to within $\pm 5\%$ (0.02 dex) of the true values and can be used in place of the templates $[C_x(\lambda) = \mathrm{fit}_x(\lambda)]$.

4.4. Comparison to WISE SFR Calibrations

The WISE All-Sky Survey (Wright et al. 2010) provided photometry for over 563 million objects, and as such has great potential for future application of our calibrations. Recently, calibrations of the WISE bands as SFR indicators have emerged (Donoso et al. 2012; Shi et al. 2012; Jarrett et al. 2013; Lee et al. 2013; Cluver et al. 2014), some of which can be easily compared to our results. In particular, we focus on the results of Jarrett et al. (2013) and Lee et al. (2013) as these have linear calibrations of the WISE 12 and 22 μm bands and can be directly compared to our values. The difference between the calibration values found in these works is rather large, corresponding to 0.34 dex ($\sim 120\%$) and 0.15 dex ($\sim 40\%$), for the WISE 12 and 22 μm band, respectively. These large discrepancies are likely the result of the different approaches of the two works. Jarrett et al. (2013) rely of the previous calibrations of Rieke et al. (2009) at 24 μm, whereas Lee et al. (2013) attempt to determine SFRs from extinction-corrected Hα emission.

The composite of our sample of SFG spectra smoothed by the WISE 12 and 22 μm filters is compared to these calibrations in Figure 6. We find that the results lie in-between the values found by Jarrett et al. (2013) and Lee et al. (2013). Since the WISE 22 μm band is so similar in shape and location to the Spitzer 24 μm band, the calibrations of Zhu et al. (2008) and Rieke et al. (2009) are also presented and show close agreement to our work.

5. APPLICATION TO HIGHER REDSHIFT GALAXIES

5.1. Demonstration

Here we demonstrate how to apply our calibrations to an SFG with a known redshift. Let us consider using the observed 24 μm flux density for the galaxy SSGSS 1 to estimate the SFR of this
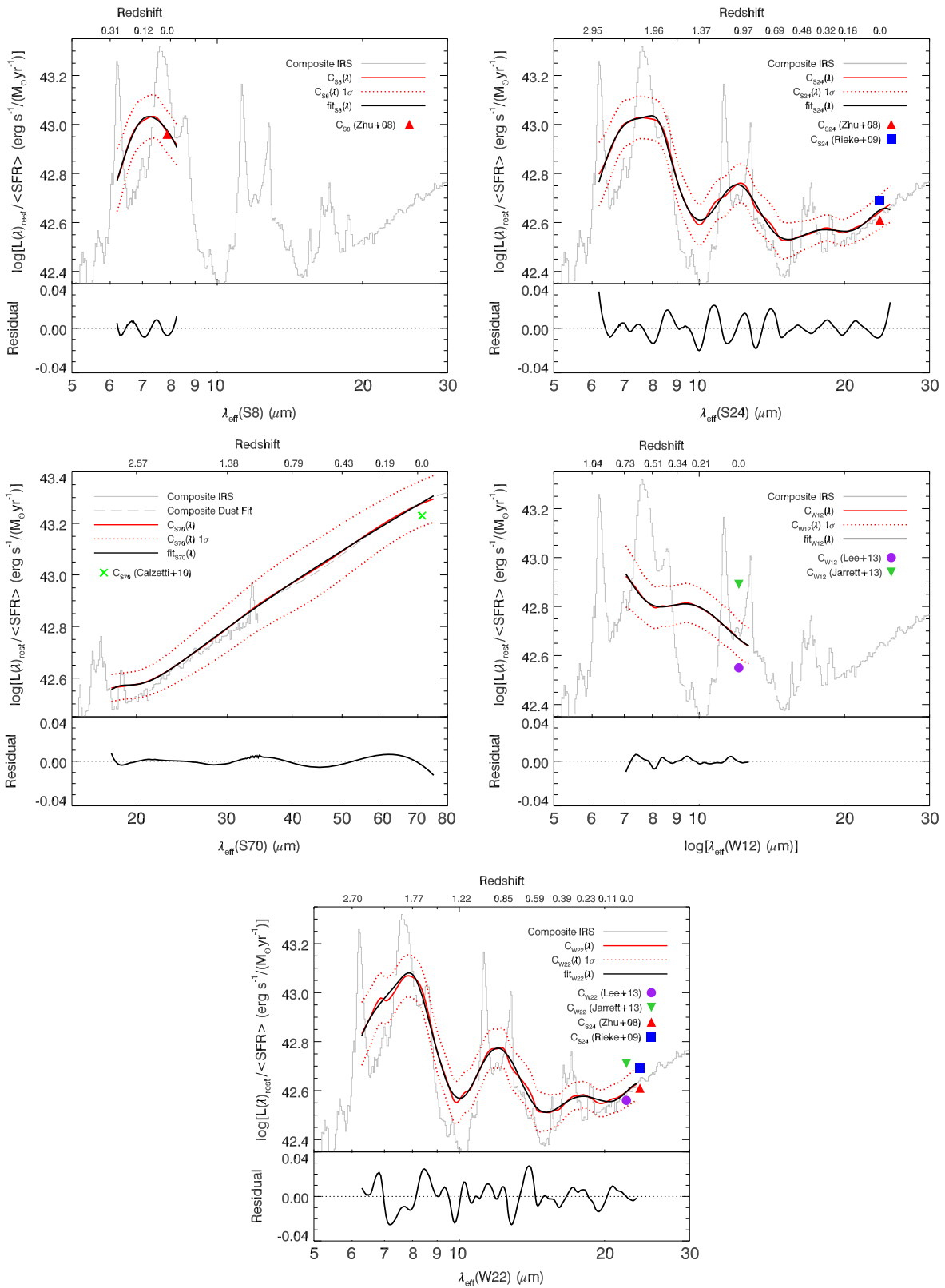
Figure 6. The top of each panel shows the conversion factor for a *Spitzer* or *WISE* band using all SFG galaxies (solid red lines), along with their uncertainty (dotted red lines), which for most cases is between 15 and 20%. The solid black line is a fit to the smoothed spectrum, $\mathrm{fit}_x(\lambda)$. Local conversion factors from the literature are also shown for comparison (colored symbols). The region below ~ 6 μm is excluded due to significantly increased uncertainty in the composite spectrum (see Section 4.2). The bottom of each panel shows the residuals between the conversion factor and a fit to the curve ($\log[C_x(\lambda)/\mathrm{fit}_x(\lambda)]$).

Table 3
Filter Properties

Instrument	Band	$\lambda_{eff,0}$ (μm)	FWHM (μm)
IRAC	8 μm	7.87	2.8
MIPS	24 μm	23.68	5.3
MIPS	70 μm	71.42	19.0
WISE	12 μm	12.08	8.7
WISE	22 μm	22.19[a]	3.5
MIRI	F1000W	10.00	2.0
MIRI	F1280W	12.80	2.4
MIRI	F1500W	15.00	3.0
MIRI	F1800W	18.00	3.0
MIRI	F2100W	21.00	5.0
MIRI	F2550W	25.50	4.0

Notes. Columns list the (1) instrument, (2) passband name, (3) rest-frame effective wavelength, and (4) FWHM.
[a] The 22 μm observations suffer from a effective wavelength error (see Wright et al. 2010; Brown et al. 2014).

galaxy. At $z = 0.066$ for this particular galaxy, the 24 μm band has an effective wavelength of $\lambda_{eff}(24) = 22.51 \, \mu$m and an observed flux density of $S_{obs}(24) = 9.72 \times 10^{-26}$ erg s^{-1} cm^{-2} Hz^{-1}, which corresponds to a luminosity of log $[L_{obs}(24)] = 43.11$ erg s^{-1}. Knowing the effective wavelength, we next want to use the composite 24 μm band smoothed spectrum to determine the appropriate conversion factor, which is found to be $\log[C_{24}(22.51 \, \mu m)] = 42.62$ erg s^{-1}/($M_\odot$ yr^{-1}) using the smoothed composite template or the fitting function (see Figure 6). Finally making use of Equation (9), we get that the SFR is simply the observed luminosity in this band divided by the conversion factor, SFR $= 10^{43.11}/10^{42.62} = 3.09 \, M_\odot$ yr^{-1}. This value differs from the actual value of $\langle SFR \rangle = 4.22 \, M_\odot$ yr^{-1} by about 30%.

Next we can consider the slightly more distant case of SSGSS 14, at $z = 0.153$, and determine the SFR from its observed 24 μm flux density of $S_{obs}(24) = 4.44 \times 10^{-26}$ erg s^{-1} cm^{-2} Hz^{-1}, which corresponds to a luminosity of $\log[L_{obs}(24)] = 43.55$ erg s^{-1}. The 24 μm band has an effective wavelength of $\lambda_{eff}(24) = 20.53 \, \mu$m, which corresponds to $\log[C_{24}(20.53 \, \mu m)] = 42.57$ erg s^{-1} ($M_\odot$ yr^{-1})$^{-1}$. Taking the ratio of these numbers gives SFR $= 9.63 \, M_\odot$ yr^{-1}. This value differs from the actual value of $\langle SFR \rangle = 9.60 \, M_\odot$ yr^{-1} by <1%.

In the same manner, each calibration can be applied to any redshift that spans the λ_{eff} range covered by IRS. These examples highlight the importance of using large sample sizes in the application of these diagnostics, as a single case can have SED variations relative to the mean of our sample, which can give rise to slight inaccuracies in SFR estimates. It is important to emphasize that the accuracy of such an application is dependent on the shape of the SED of SFGs as a function of redshift. The extent to which this condition holds is examined in detail in Section 6.2.

5.2. Limitations of this Sample

It is important to acknowledge the potential differences of this sample with respect to high-z galaxies as well as the limitations for its use. As was mentioned, the selection criteria for the SSGSS sample limit it to relatively high metallicities, which may not be a well representative sample

as one goes to high-z. In addition, if the dust content of high-z galaxies is different, it is possible that the amount of UV light reprocessed by dust could change. For example, if high-z galaxies had more dust, then our templates would over-estimate the SFR, as it would be implicitly adding back in unobscured UV flux present in the SSGSS sample but that may not be there for the high-z galaxies. Variations in the typical dust temperature of galaxies with redshift would also pose a problem, as this would result in variations in their FIR SED. The relative importance of some of these effects will be tested when we compare our SED to those at higher redshift (Section 6.2).

Another area for concern is in the range of L_{IR} values spanned by the SSGSS sample. Our template is made utilizing galaxies over a range of $9.53 \leqslant \log(L_{IR}/L_\odot) \leqslant 11.37$, which is lower than the range that is currently accessible at high-z. However, the results of Elbaz et al. (2011) suggest that luminous infrared galaxies (LIRGs; $L_{IR} > 10^{11} L_\odot$) and ultra-luminous infrared galaxies (ULIRGs; $L_{IR} > 10^{12} L_\odot$) identified in the GOODS-*Herschel* sample at high-z have similar SEDs to normal SFGs, in contrast to their SB-like counterparts found locally (e.g., Rieke et al. 2009). They find that the entire population of IR-bright galaxies has a distribution with a median of IR8 $= L_{IR}/L_{rest}(8\mu m) = 4.9[-2.2, +2.9]$, where the term in brackets is the 1σ dispersion. Elbaz et al. 2011 suggest that this population can be separated into two groups: a main-sequence (MS) of normal SFGs for which IR8 $= 4 \pm 2$ consisting of ∼80% of the population, and SB galaxies which occupy the region with IR8 > 8 and represent about ∼20% of the population. For reference, the IR8 value of our template is 4.8, which agrees with the median of the GOODS-*Herschel* sample. The uniformity of IR8 values in MS galaxies, over the range $10^9 < L_{IR}/L_\odot < 10^{13}$, suggests that the SED of normal SFGs do not change drastically with luminosity. This also indicates that our limited range in L_{IR} coverage for the SSGSS sample should not drastically affect its utility toward higher luminosity MS galaxies.

Perhaps the biggest factor limiting the large scale application of this technique is in the ability to identify galaxy types at higher redshifts. The calibrations presented in this work are applicable to normal SFGs, typically referred to as being on the MS of star formation, and not to cases undergoing SB activity (different SED) or with AGNs (significant IR emission not associated with star formation). This topic should be thoroughly addressed before widespread applications of these calibrations can be made to specific surveys.

There are a several techniques that have been demonstrated to isolate out AGN and SB galaxies; however, some of them rely on observations made outside the MIR. One of the most reliable techniques to identify AGNs is through X-ray observations (e.g., Alexander et al. 2003), however these can miss obscured AGNs and could be biased (Brandt & Hasinger 2005). In order to avoid obscuration effects, AGN selection techniques using the MIR and FIR have also been developed. These include *Spitzer*+*Herschel* color-cuts (Kirk-patrick et al. 2012), *Spitzer*/IRAC color-cuts (Lacy et al. 2004; Stern et al. 2005; Donley et al. 2012; Kirkpatrick et al. 2012), and *WISE* color-cuts (Mateos et al. 2012; Stern et al. 2012; Assef et al. 2013). Emission line diagnostics, such as the BPT diagram (Kewley et al. 2013a) and the Mass–Excitation diagram (Juneau et al. 2014), are also effective techniques. It
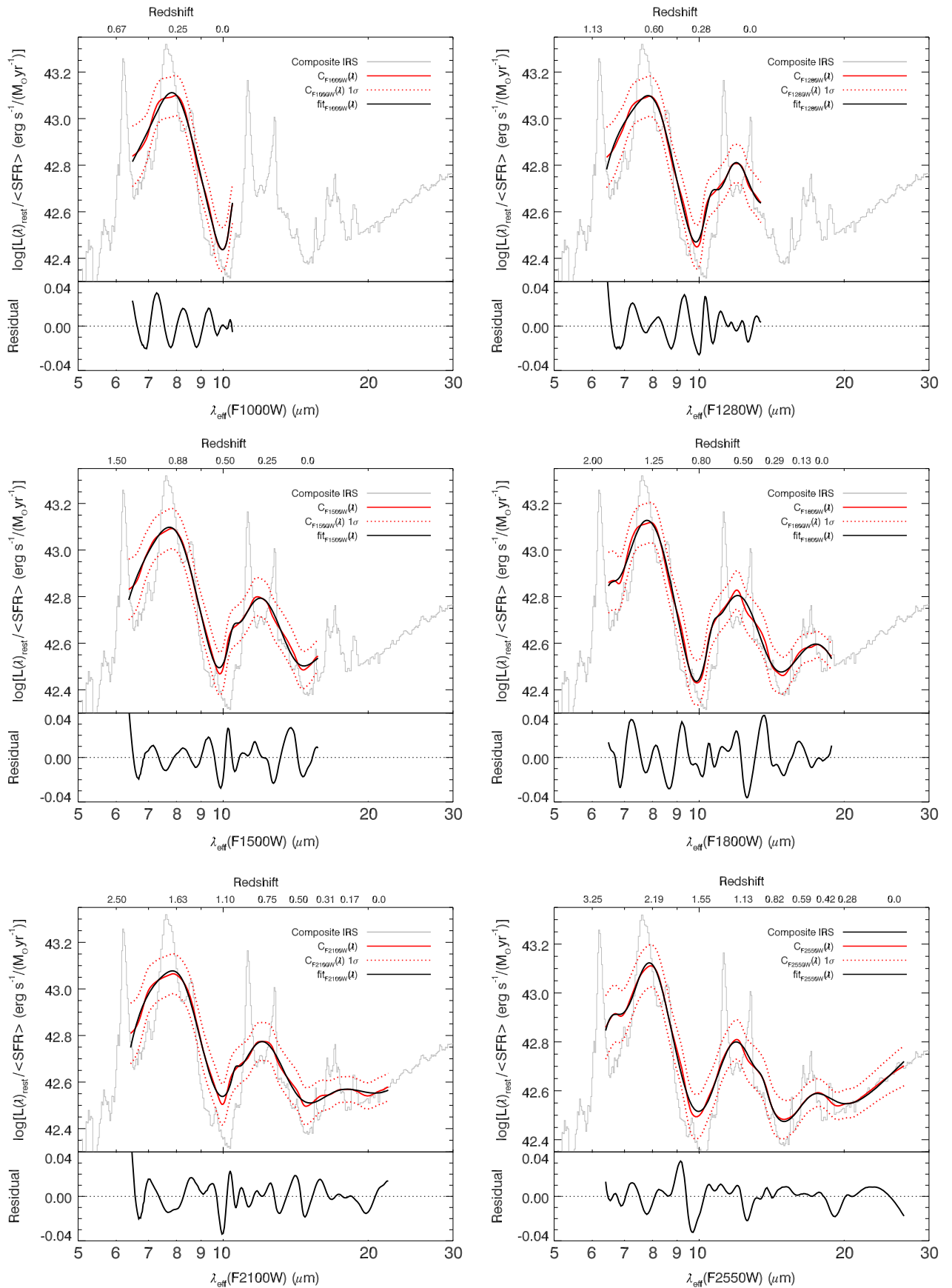
Figure 7. The top of each panel shows the conversion factor for select *JWST*/MIRI bands using all SFG galaxies (solid red lines), along with their uncertainty (dotted red lines), which for most cases is between 15 and 20%. The region below ∼6 μm for each band is excluded due to significantly increased uncertainty in the composite spectrum (see Section 4.2). The bottom of each panel shows the residuals between the conversion factor and a fit to the curve ($\log[C_x(\lambda)/\mathrm{fit}_x(\lambda)]$).

Table 4
Continuous Star Formation Rate Calibration $\text{fit}_x(\lambda)$ Parameters

Band	λ_{eff} Range (μm)	z Limit	p_1	p_2	λ_1 (μm)	b_1	γ_1	λ_2 (μm)	b_2	γ_2	λ_3 (μm)	b_3	γ_3	λ_4 (μm)	b_4	γ_4	λ_5 (μm)	b_5	γ_5
$S8$	6.20–7.87	0.27	−1.229e42	⋯	7.1	1.075e43	0.349	8.2	3.102e42	0.224	⋯	⋯	⋯	⋯	⋯	⋯	⋯	⋯	⋯
$S24$	6.20–23.68	2.82	−2.803e42	⋯	7.1	1.107e43	0.413	8.2	4.496e42	0.165	12.0	5.300e42	0.341	17.9	4.154e42	0.576	25.0	5.093e42	0.366
$S70$	17.85–71.42	3.00	−3.213e42	3.125e41	17.9	1.208e42	0.272	⋯	⋯	⋯	⋯	⋯	⋯	⋯	⋯	⋯	⋯	⋯	⋯
$S70_{\text{corr}}$	17.85–71.42	3.00	−1.929e42	2.825e41	35.0	4.065e42	0.461	47.0	2.029e42	0.732	⋯	⋯	⋯	⋯	⋯	⋯	⋯	⋯	⋯
$W12$	7.00–12.08	0.73	−1.598e43	1.112e42	6.3	1.528e43	0.402	9.5	9.050e42	0.685	⋯	⋯	⋯	⋯	⋯	⋯	⋯	⋯	⋯
$W22$	6.28–22.19	2.53	−1.791e43	⋯	6.8	2.253e43	0.789	8.0	6.473e42	0.198	12.0	9.557e42	0.392	17.9	1.428e43	0.743	25.0	1.202e43	0.401
$F1000W$	6.48–10.00	0.54	−2.463e42	⋯	6.7	6.078e42	0.569	7.9	1.074e43	0.247	10.6	4.042e42	0.065	⋯	⋯	⋯	⋯	⋯	⋯
$F1280W$	6.43–12.80	0.99	−5.267e43	3.409e42	6.7	3.544e43	0.801	8.0	7.603e42	0.224	10.6	2.468e42	0.097	11.9	6.918e42	0.213	⋯	⋯	⋯
$F1500W$	6.37–15.00	1.35	−2.105e43	⋯	6.7	2.212e43	0.756	7.9	1.038e43	0.285	10.5	1.359e42	0.069	11.9	1.174e43	0.367	17.7	1.976e43	0.684
$F1800W$	6.48–18.00	1.78	−1.339e43	3.510e41	6.4	8.470e42	0.160	7.8	2.092e43	0.317	10.7	1.581e42	0.082	12.0	1.008e43	0.331	17.7	8.963e42	0.539
$F2100W$	6.43–21.00	2.27	−1.493e43	6.926e41	7.0	1.531e43	0.483	8.1	7.937e42	0.247	10.6	8.052e41	0.048	12.0	8.089e42	0.357	17.3	4.146e42	0.533
$F2550W$	6.40–25.50	2.99	−6.947e42	4.408e41	6.5	7.568e42	0.186	7.9	1.468e43	0.237	11.9	6.429e42	0.273	13.5	8.379e41	0.083	17.3	2.112e42	0.290

Notes. The second fit for $S70$ has a correction term that takes into account the FIR variation of SFG SEDs with redshift (see Section 6.3). The functional form of these fits is $f_{\text{IRS}}(\lambda) = \sum_{i=1}^{2} p_i \lambda^{(i-1)} + \sum_{r=1}^{5} I_r(\lambda)$, where

$$I_r(\lambda) = \frac{b_r \gamma_r^2}{(\lambda/\lambda_r - \lambda_r/\lambda)^2 + \gamma_r^2}.$$

has been suggested that SB galaxies can be identified as sources with IR8 > 8 by Elbaz et al. (2011).

6. DISCUSSION

6.1. Origins of the Scatter in SFR(λ)

In addition to grouping all of the SFGs together, we also examine grouping our galaxies based on their luminosity at rest-frame 3.6, 4.5, 8, 24, and 70 μm, as well as their L_{IR}, L_{IR} surface brightness, and $L(H\alpha)/L(24\,\mu m)$ ratios, in order to identify possible origins to the scatter within the SFR calibration of the entire group. These bands are chosen because 3.6 and 4.5 μm correlate with the underlying stellar population (i.e., stellar mass; Meidt et al. 2012, 2014), and the other bands correlate strongly with star formation (Zhu et al. 2008; Rieke et al. 2009; Calzetti et al. 2010; Hao et al. 2011). For each of these cases, the sample is divided into six bins with 9–10 galaxies in each.

Looking at each of the calibrations, weak trends are found suggesting larger conversion factors, at almost all MIR wavelengths, for galaxies with higher luminosities when arranged by any of the luminosities mentioned before. A few examples are shown in Figure 8. These trends are very weak because the separation between the groups is comparable to the scatter within each of the groups, which is 10–25% (the largest scatter at lowest luminosity galaxies), and similar to the uncertainty of the entire group average values. If real, these trends could suggest that (1) galaxies with a larger old stellar population require slightly larger conversion factors at all MIR wavelengths, as might be expected if light unassociated to star formation is contaminating the MIR; and/or (2) a slightly super-linear relationship exists between luminosity and SFRs in the MIR.

Our attempts to account these effects by introducing additional terms into the conversion factors do not appear to significantly reduce the overall scatter of the conversion factors. Such additional terms would also make application of this method to higher redshift galaxies more difficult, as more information would be needed (e.g., determination of rest-frame luminosities). Given our limited range in galaxy properties to determine the validity of any trends, we adopt the simplest approach and use the entire group average for our analysis. We refrain from using higher luminosity local galaxies, such as the (U)LIRGs in the GOALS sample (Armus et al. 2009), as an additional test of such claims because of the significant FIR SED evolution that occurs for $L_{IR} \gtrsim 10^{11} L_{\odot}$, which is absent from galaxies of these luminosities at high-z (see Section 5.2; Elbaz et al. 2011). In addition, a large fraction of these systems are likely to host AGNs (U et al. 2012), which would be excluded by our selection process. For reference to the reader, we illustrate the local SED evolution by comparing the GOALS photometry (U et al. 2012) and a few of the Rieke et al. (2009) templates to our own template, normalized by $L_{rest}(8\,\mu m)$, in Figure 9.

6.2. Variation in SFG SEDs with Redshift

Many studies have sought to characterize the SED of different galaxy types (e.g., SFG, AGN) as functions of redshift. In this section, the templates of Elbaz et al. (2011); Kirkpatrick et al. (2012); Magdis et al. (2012) and Ciesla et al. (2014) are compared to our own to thoroughly examine the extent to which the SED of SFGs change with redshift. Similar

to the approach outlined in this work, these studies use large surveys to construct IR templates for different populations of galaxies at different redshifts. In general, the templates created in these studies suggest that the mean dust temperature of galaxies increases as one looks to higher redshifts. In addition to the change in dust temperature that is evident, Magdis et al. (2012) suggest that the value of IR8 increases mildly from IR8 ∼4 to IR8 ∼ 6 at $z > 2$ for MS galaxies.

If one considers the notion that both $L_{rest}(8\,\mu m)$ and L_{IR} are typically used for SFR indicators, such a change in IR8 would suggest that there is a change in the SFR converstion factor of one (or both) of these luminosities with redshift and this is important to keep in mind when comparing the templates. Changes in $L_{rest}(8\,\mu m)$ could result from variations in PAH abundances relative to the total dust content, which has been found to correlate with metallicity (Engelbracht et al. 2005, 2008; Marble et al. 2010), and also to the hardness of the radiation field (Madden et al. 2006; Engelbracht et al. 2008; Gordon et al. 2008). Given the sensitivity of L_{IR} to the contributions from older stellar populations (Calzetti et al. 2010), it is also likely that the value of the conversion factor for SFR-L_{IR} could also vary with redshift.

The comparison between the templates from the literature to our own is shown in Figures 10 and 11. We have chosen to normalize the templates in two ways, both of which correlate with star formation. Normalizing by a close proxy for star formation is crucial to compare how viable our continuous calibrations are at higher redshifts. The first method is to normalize by $L_{rest}(8\,\mu m)$, which is chosen over use of the 24 μm region because it is not available for the Kirkpatrick et al. (2012) templates. With this choice of normalization, it is also easier to directly compare the shape of the MIR SEDs. The second method is to normalize by L_{IR}, as is traditionally done in many template comparisons. We reemphasize that the observed trend of IR8 increasing from 4 to 6 implies that these choices of normalization for the templates will give different results.

First, the templates of Kirkpatrick et al. (2012) are examined as these provide the best sample for comparison because they are based on direct spectral measurements of higher redshift galaxies. In addition, access to spectral data allowed them to accurately identify galaxies with significant AGN contribution and create separate templates for AGNs and SFGs, the latter of which are considered here. The gap in spectral coverage of their templates, shown as the vertical dotted lines in Figure 10, correspond to regions lacking spectral or photometric values with which to constrain the SED, and is ignored for our comparison. Looking at the templates normalized by $L_{rest}(8\,\mu m)$, it is seen that the templates show remarkable agreement in SED shape for $\lambda < 24\,\mu m$ and lie almost entirely within the scatter in our local SED template. In contrast, there is clear disagreement in SED shape at $\lambda > 24\,\mu m$ which becomes more drastic at higher redshift. This is mostly due to the larger IR8 values of these templates, which exceed the IR8 values observed in photometric samples at these redshifts (Magdis et al. 2012). For reference, the Kirkpatrick et al. (2012) $z \sim 1$ template has IR8 = 6.5 and the $z \sim 2$ template has IR8 = 8.0. We associate this difference to the selection criteria of this sample, which required bright sources at 24 μm ($S_{24} > 100\,\mu Jy$) to obtain IRS spectroscopy and which corresponds to more L_{IR} luminous galaxies at higher redshifts (see Section 6.4 for more details). When instead normalized by
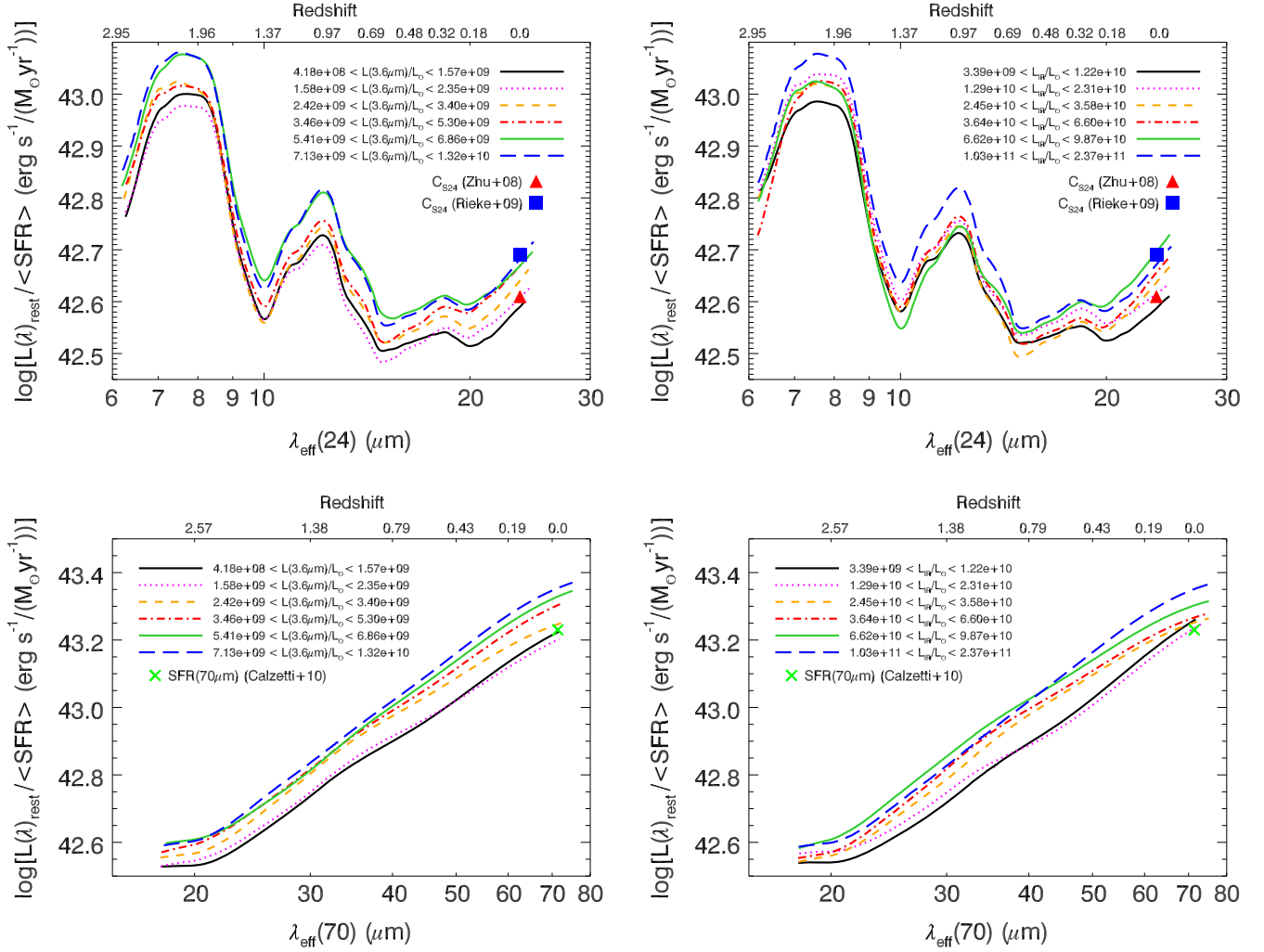
Figure 8. Top: $C_{24}(\lambda)$ conversion factor for galaxies when arranged into groups (∼10 galaxies) according to $L(3.6\ \mu m)$, a proxy for stellar mass, and L_{IR}, a proxy for the SFR. Bottom: $C_{70}(\lambda)$ conversion factor for galaxies when arranged according to $L(4.5\ \mu m)$ and L_{IR}. Local conversion factors are also shown for comparison. The dispersion in each of the groups (between 10 and 25%; see Section 6.1) is not shown for clarity, but is comparable to the separation among the groups. Weak trends appear which would suggest larger conversion factors are needed for the higher luminosity galaxies.
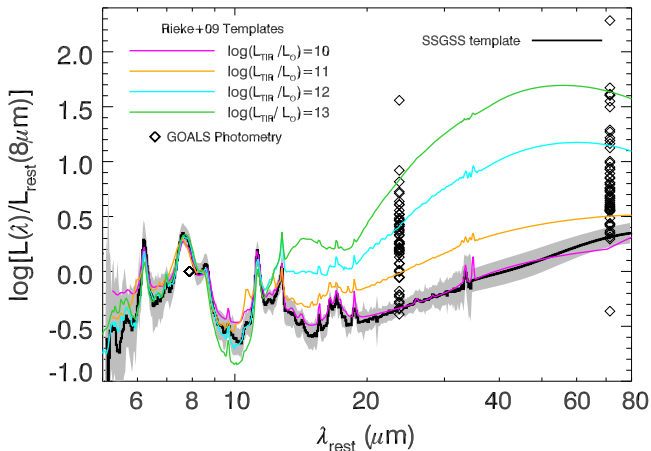
Figure 9. Comparison of our SFG composite template to GOALS photometry (U et al. 2012) and Rieke et al. (2009) templates. The scatter of the SSGSS template is shown as the filled gray region. The values of IR8 = $L_{IR}/L_{rest}(8\mu m)$ for the Rieke et al. (2009) templates range from IR8 = 4.8 at $L_{TIR} = 10^{10}L_\odot$ to IR8 = 59.6 at $L_{TIR} = 10^{13}L_\odot$, whereas high-z galaxies over this luminosity range have IR8 = 4.9[−2.2, + 2.9] (Elbaz et al. 2011). Therefore, there is significant FIR SED evolution that occurs for local (U) LIRGS that is absent at high-z.

L_{IR}, slight offsets appear between the templates for $\lambda < 24\ \mu m$ as a result of the larger L_{IR} with increasing redshift. The fact that the shape remains fixed, regardless of possible offsets, gives credibility to this technique being applicable to up to $z \sim 2$ for all bands at effective wavelengths below 24 μm. In contrast, even when normalized by L_{IR} there is clear disagreement in SED shape at $\lambda > 24\ \mu m$ which becomes more drastic at higher redshift. This effect, also observed by Magdis et al. (2012), is argued to be due to the mean dust temperature of galaxies increasing with redshifts.

There are multiple physical mechanisms that give rise to increased dust temperatures in galaxies. Locally, similar trends are seen in galaxies with increasing values of L_{IR} (e.g., Rieke et al. 2009). However, for local LIRGs and ULIRGs there is also an associated decrease in the relative strength of the 8 μm PAH feature relative to the FIR, corresponding to IR8 values more similar to SB galaxies, which deviates significantly from our template. Instead, Magdis et al. (2012) suggest that this could be the result of a hardening of the radiation field, $\langle U \rangle$, in MS galaxies with increasing redshift ($\langle U \rangle \propto (1 + z)^{1.15}$). Adopting Draine & Li (2007) models to fit their galaxy SEDs, for which $\langle U \rangle \propto L_{IR}/M_{dust}$, they argue that this is explained by
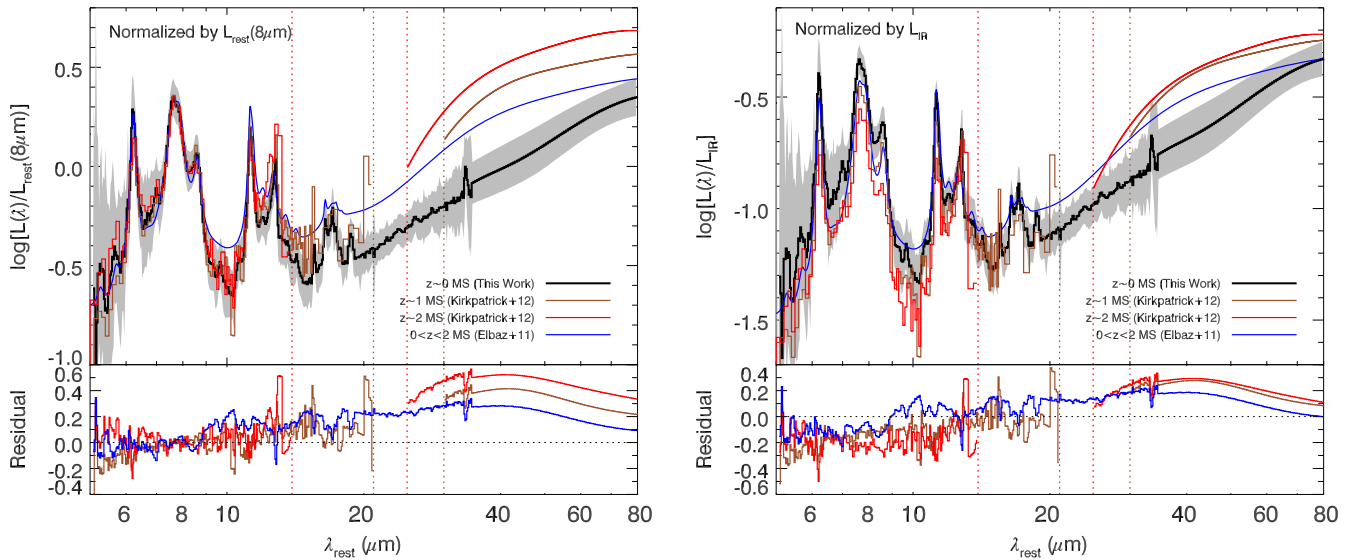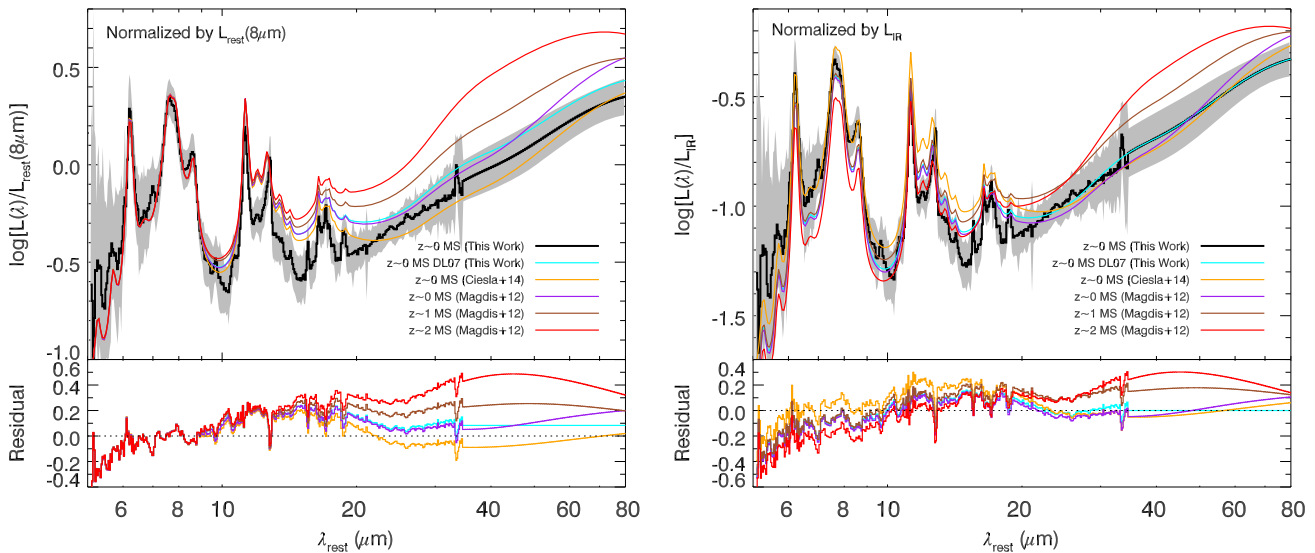
Figure 10. The top of each panel shows the comparison of the composite SED of SFGs in our sample to those at higher redshifts for which spectroscopic information is available. The scatter of the SSGSS template is shown as the filled gray region. The SEDs have been normalized by $L_{rest}(8\ \mu m)$ and L_{IR}. The sections between the vertical dotted green and red lines, corresponding to the $z \sim 1$ and $z \sim 2$ templates from Kirkpatrick et al. (2012), lack spectral data. The template of Elbaz et al. (2011) uses redshifted photometry to act as a spectroscopic analog. The bottom of each panel shows the residuals between our template and the other templates. The shape of the SED remains unchanged with redshift for $\lambda \lesssim 20\ \mu m$, with only constant offsets occurring depending on the normalization. For $\lambda \gtrsim 20\ \mu m$, significant SED evolution is present with increasing redshift.

Figure 11. The top of each panel shows the comparison of the composite SED of SFGs in the SSGSS sample to those at higher redshifts for which Draine & Li (2007) models have been used to fit the available photometry. The scatter of the SSGSS template is shown as the filled gray region. The SEDs have been normalized by $L_{rest}(8\ \mu m)$ and L_{IR}. Note that when normalized by $L_{rest}(8\ \mu m)$ these model-based template have an excess in the 10–25 μm region compared to the spectral data. This trend is seen in our own fits of Draine & Li (2007) models (cyan line), and indicates a limitation in the simple three-component model typically adopted (see Section 3.2). The bottom of each panel shows the residuals between our template and the other templates.

the redshift evolution of the $M_* - Z$ and SFR $- M_*$ relations. Another physical mechanism that gives rise to this effect is compactness. More compact star formation in galaxies can give rise to elevated dust temperatures and appears to occur more frequently in MS galaxies at higher redshifts (Elbaz et al. 2011; Schreiber et al. 2014). Regardless of the origin of this effect, these results suggest that the 70 μm band requires additional correction to be utilized as an SFR diagnostic as a function of redshift. We perform this analysis in the next section.

Next, the templates of Elbaz et al. (2011) are considered. These templates make use of redshifted photometry of galaxies from $0 < z < 2$ to act as a spectroscopic analog. The

combination of all galaxies over this redshift range of results in an artificially broad FIR bump, due to the shifting of the FIR bump with z, and makes direct comparison of these templates tricky. In general there is good agreement in SED shape with their MS template and our own if this FIR broadening is taken into account.

Lastly, the templates based on Draine & Li (2007) model fitting of photometric data are considered, shown in Figure 11. These include the templates of Magdis et al. (2012), and Ciesla et al. (2014). Considering first the $z \sim 0$ cases normalized by $L_{rest}(8\ \mu m)$, we note that all of these model-based templates show the same excess in the 10–25 μm region compared to the
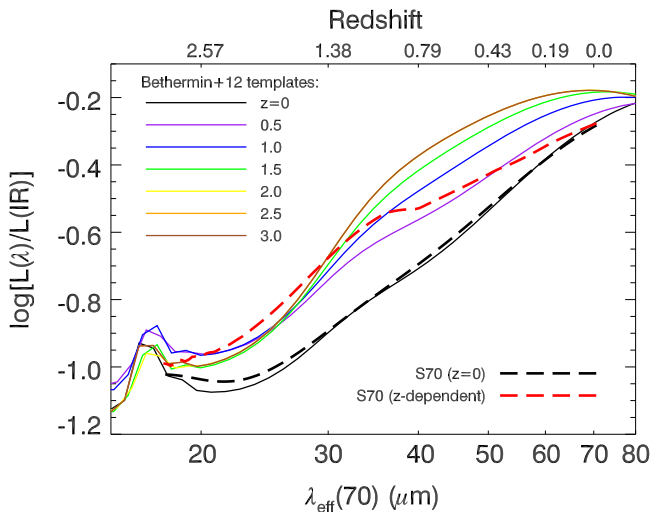
Figure 12. The SED of SFGs changes with redshift, as demonstrated by the templates of Béthermin et al. (2012). Taking this into account, the value of $C_{70}(\lambda)$ would change significantly from those derived from a $z \sim 0$ SED (dashed black line). This change is demonstrated as the red dashed line, which shows the 70 μm filter convolution when accounting for the SED variations with redshift. We stress that the red dashed line is a z-dependent interpretation of the expected 70 μm emission and cannot be considered a spectrum for an individual galaxy.

spectral data that was seen in our own fits using Draine & Li (2007) models (cyan line in the Figure 11). This suggests that these model-based templates may not be accurately representing the intrinsic SED over this region. The region beyond 25 μm is likely to be more representative, as it is usually well fit a simple two-component dust model. As with the spectral-based templates, the FIR bump peaks at shorter wavelengths with increasing redshift and also shows an increase in IR8.

Taken together, it would appear that there is no strong evidence to suggest that the shape of the SED for SFGs varies significantly over the wavelength region of 6–30 μm. However, vertical offsets, corresponding to a constant factor offset, cannot be ruled out without direct comparison of SFR estimates for higher redshift galaxies.

6.3. Accounting for Dust Temperature Variation

The significant change in shape of the FIR bump makes the calibrations at the longer wavelengths (i.e., $C_{70}(\lambda)$) more difficult. Comparing the SED of the higher-z galaxies at these wavelengths to the SSGSS SED, there is a significant difference (up to 0.5 dex), which exceeds the scatter of SEDs for local SFGs. For this reason, a correction to $C_{70}(\lambda)$ does appear necessary if it is to be applied at higher redshifts.

We correct for the dust temperature variation using the the SED template grids of Béthermin et al. (2012), which are built from the results of Magdis et al. (2012). These templates have been normalized by L_{IR}. By making use of this grid, the observed *Spitzer* 70 μm luminosity as function of redshift is estimated while accounting for the changing SEDs. A demonstration of how the observed luminosity changes is shown in Figure 12. For example, at $z = 0.5$ and $z = 1$ the 70 μm band measures rest-frame 46.7 and 35.7 μm, respectively, and the observed band luminosity is derived from the $z = 0.5$ (purple line) and $z = 1$ (blue line) templates at those wavelengths. We perform a fit to this new conversion factor

and present it in Table 4. The accuracy of this correction will be tested in the following section.

6.4. Testing the Calibrations

To test the utility of our calibrations, we compare SFRs of galaxies from other surveys to those found using our continuous, monochromatic values developed in this work. This requires a survey which has photometry available in one of the calibrated bands, as well as an independent technique to measure star formation from the those used to calibrate our conversion factors. We choose to use SFRs based on L_{IR} measurements as these are the most readily available diagnostic for deep IR surveys. For consistency with our local SSGSS sample, we adopt a conversion factor of $\log[C(L_{IR})] = 43.64 \, \text{erg s}^{-1} \, (M_\odot \, \text{yr}^{-1})^{-1}$, which corresponded to a $\tau \sim 500$ Myr constant star formation (see Section 3.5). Furthermore, sources with significant AGN components need to be to identified and removed. It is worth noting that adopting different L_{IR} conversion factors for this analysis will only lead a constant offset between these two SFRs at all redshifts and that we are most interested in assessing where breaks from a constant relation develop.

First we use the sample of 70 sources identified as SFGs from Kirkpatrick et al. (2012), corresponding to an AGN contribution of less than 20%. These galaxies cover a redshift range of $0.3 < z < 2.5$ and have full *Spitzer* and *Herschel* photometry. We use the L_{IR} measurements of these galaxies from Kirkpatrick et al. (2012) (private communication), determined from IRS measurements for the MIR and by fitting two modified blackbodies for the FIR. A comparison of SFR $(C_{24}(\lambda))$ to SFR(L_{IR}) is shown in Figure 13, both as a function of redshift and L_{IR}. There is general agreement between the values up to redshifts of about $z \sim 1$, which corresponds to galaxies with $\log[L_{IR}/L_\odot] < 12$. Given that the sources of Kirkpatrick et al. (2012) were required to be very bright in the IR to obtain IRS spectral measurements at these redshifts, it is likely that their sources at $z > 1$ are slightly biased to larger L_{IR} luminosities (demonstrated by their larger IR8 values). These values deviate significantly from deeper photometric surveys of SFGs at these redshifts, which is shown in Figure 13, by the templates of Magdis et al. (2012) (dashed cyan line). We remind the reader that the Magdis et al. (2012) templates are based on Draine & Li (2007) models, which was found to show significant offsets compared to the observed spectra of the SSGSS galaxies, and is only shown for reference. We also examine the comparison of SFR($C_{70}(\lambda)$) to SFR(L_{IR}), shown in Figure 14. The redshift-dependent correction of $C_{70}(\lambda)$ seems to work well for galaxies of $z \lesssim 1.2$, for which data is available for this band.

As a second test we use the sample from Elbaz et al. (2011). This sample covers a redshift range of $0.03 < z < 2.85$ and has *Spitzer* and *Herschel* photometry. The L_{IR} values for these galaxies have been determined by Schreiber et al. (2014), and are estimated from the Chary & Elbaz (2001) template that provides the best fit to the *Herschel* data. For our analysis we only consider sources for which at least one photometric band covers wavelengths greater than 30 μm, as these cases achieve better accuracy of the FIR region. The photometric redshifts of these sources are obtained from Pannella et al. (2014) (using the EAZY code; Brammer et al. 2008), and we require the sources to have suitable quality flags. These photometric redshifts achieve a relative accuracy (that is,
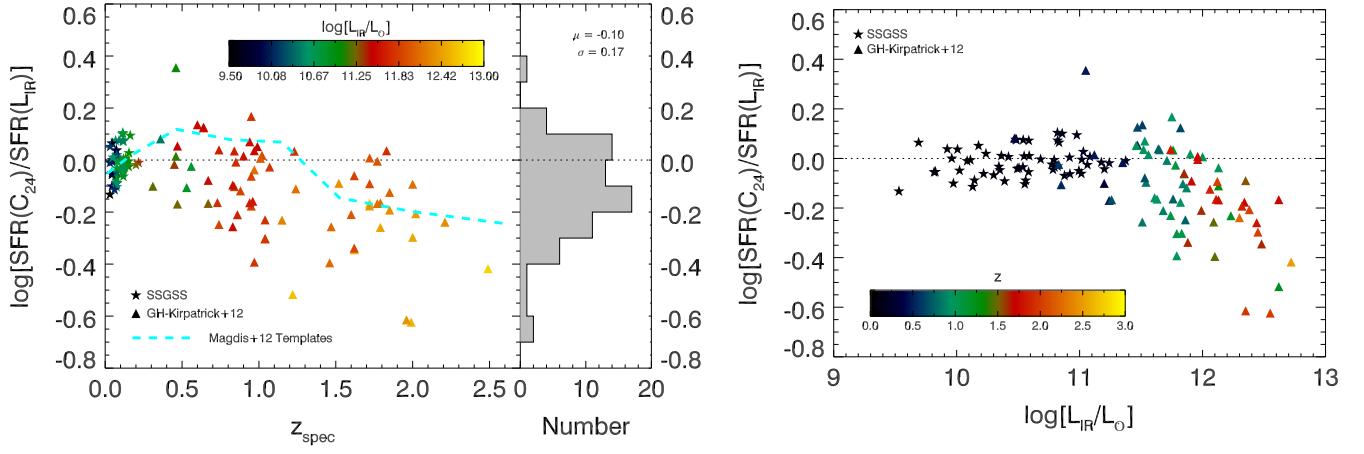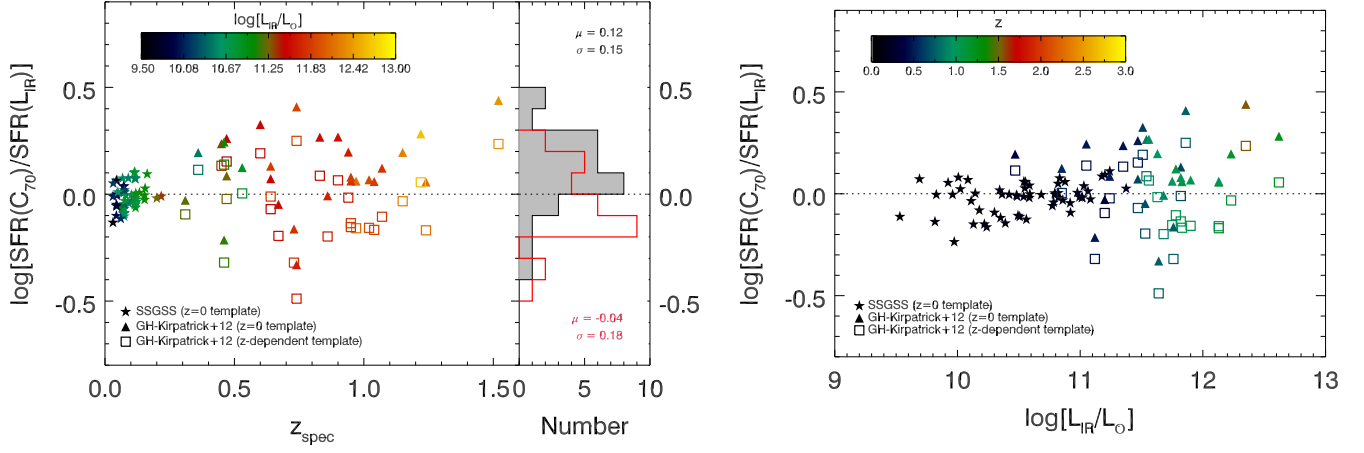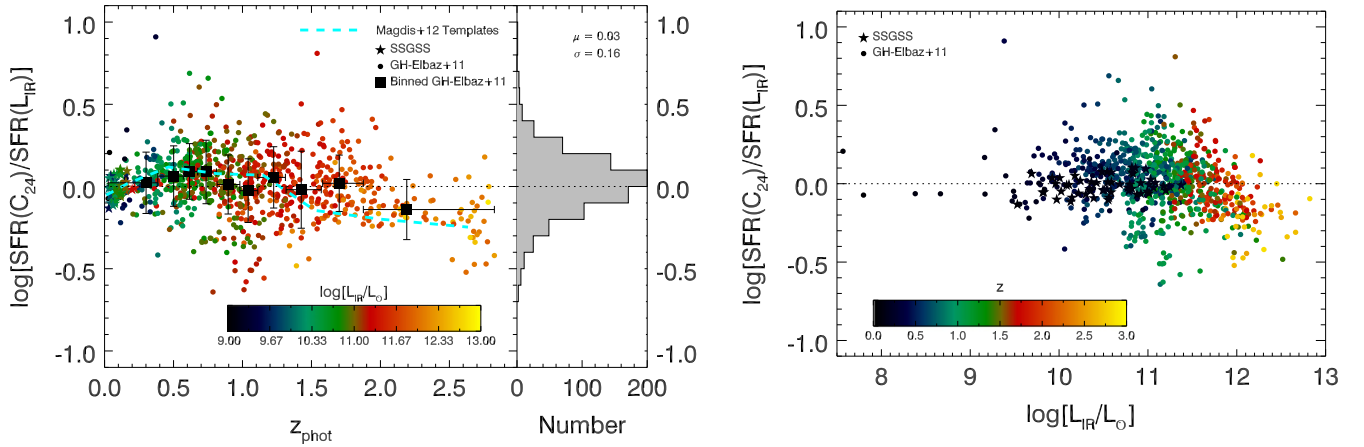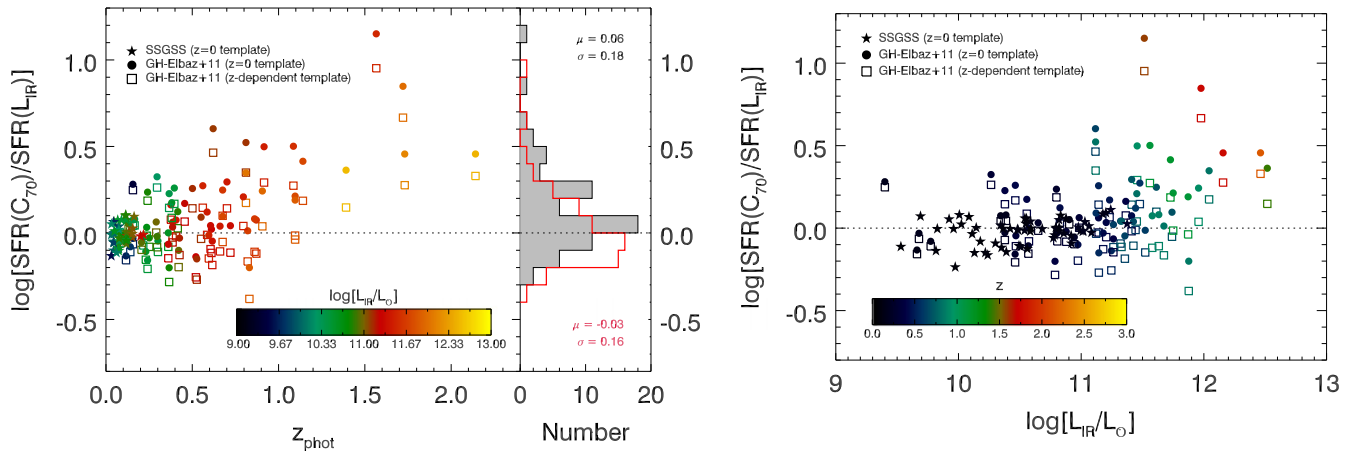
Figure 13. Comparison of SFRs estimated from $C_{24}(\lambda)$ and L_{IR} for the GOODS-*Herschel* sample from Kirkpatrick et al. (2012). Left: comparison as a function of redshift. The values show agreement for $z \lesssim 1$, beyond which the dataset is biased toward galaxies with $\log[L_{IR}/L_\odot] \gtrsim 12$. The distribution of the Kirkpatrick et al. (2012) sources, along with the parameters of a best-fit Gaussian to this distribution, is also shown. Right: comparison as a function of L_{IR}. The values show agreement for cases with $\log[L_{IR}/L_\odot] \lesssim 12$. For cases with $\log[L_{IR}/L_\odot] \gtrsim 12$, which dominate $z \gtrsim 1$ for this sample, the monochromatic SFR is lower than the L_{IR} SFR.

Figure 14. Comparison of SFRs estimated from $C_{70}(\lambda)$ and L_{IR} for the GOODS-*Herschel* sample from Kirkpatrick et al. (2012). Left: comparison as a function of redshift when using our calibration based on a $z = 0$ template (filled triangles) and the z-dependent template (open squares). The calibration derived from the z-dependent template appears to work better than the $z = 0$ template and shows agreement for $z \lesssim 1.2$, beyond which data are lacking. The distributions of the Kirkpatrick et al. (2012) sources when using the $z = 0$ template (filled gray) and z-dependent template (open red), along with the parameters of a best-fit Gaussian to these distributions, are also shown. Right: comparison as a function of L_{IR}.

Figure 15. Comparison of SFRs estimated from $C_{24}(\lambda)$ and L_{IR} for the GOODS-*Herschel* sample from Elbaz et al. (2011). Left: comparison as a function of redshift. The values show agreement for $z \lesssim 2$, beyond which the dataset is biased toward galaxies with $\log[L_{IR}/L_\odot] \gtrsim 12$. The distribution of the Elbaz et al. (2011) sources, along with the parameters of a best-fit Gaussian to this distribution, is also shown. Right: comparison as a function of L_{IR}. The values show reasonable agreement for cases with $\log[L_{IR}/L_\odot] \lesssim 12$. For cases with $\log[L_{IR}/L_\odot] \gtrsim 12$, which dominate $z \gtrsim 2$ for this sample, the monochromatic SFR is lower than the L_{IR} SFR.

Figure 16. Comparison of SFRs estimated from $C_{70}(\lambda)$ and L_{IR} for the GOODS-*Herschel* sample from Elbaz et al. (2011). Left: comparison as a function of redshift when using our calibration based on a $z = 0$ template (filled triangles) and the z-dependent template (open squares). The calibration derived from the z-dependent template appears to work better than the $z = 0$ template and shows agreement for $z \lesssim 1$, beyond which data are lacking. The distributions of the Elbaz et al. (2011) sources when using the $z = 0$ template (filled gray) and z-dependent template (open red), along with the parameters of a best-fit Gaussian to these distributions, are also shown. Right: comparison as a function of L_{IR}.

$\Delta z = (z_{phot} - z_{spec})/(1 + z_{spec}))$ of 3%, with less than 3% of cases suffering from catastrophic failures ($\Delta z > 0.2$; Pannella et al. 2014). These sources lack spectroscopic measurements to identify AGN or SB sources and we rely on the color-cut outlined by Kirkpatrick et al. (2012) for AGNs and also remove sources with IR8 > 8 from our sample, which are believed to be predominately SB galaxies (Elbaz et al. 2011). We follow the method of Elbaz et al. (2011) to determine rest-frame 8 μm from k-correcting the 8 μm band ($z < 0.5$), 16 μm band ($0.5 < z < 1.5$), and 24 μm band ($1.5 \leqslant z \leqslant 2.5$) assuming these galaxies follow the IR SED of M82. These constraints leave us with an SFG sample of 825 sources with 24 μm observations and 66 with 70 μm observations.

Using the measured L_{IR} values from these sources, the same comparison is made as before and is shown in Figure 15. In this case there appears to be more agreement among the diagnostics out to redshifts of $z \lesssim 2$, with a 1σ dispersion of 0.16 dex (45%). Small changes appear to develop beyond $z > 2$, which is consistent with the observed trend of IR8 going 4 to 6 by $z = 3$ (a difference of ~0.2 dex). This trend is apparent in the ratios of observed 24 μm luminosity to L_{IR} in the templates of Magdis et al. (2012) (dashed cyan line). Similar to the Kirkpatrick et al. (2012) sample, the largest discrepancies occur in galaxies with $\log[L_{IR}/L_\odot] > 12$. Next, we examine the comparison of SFR($C_{70}(\lambda)$) to SFR(L_{IR}) shown in Figure 16. As before, the redshift-dependent correction of $C_{70}(\lambda)$ seems to work well for galaxies of $z \lesssim 1$, with a 1σ dispersion of 0.18 dex (50%). For $z \gtrsim 1$, significant differences appear but this is likely due to the poor sensitivity of the 70 μm band detecting only the most luminous galaxies in these bands at high redshifts. With the limited number of sources available at $z > 1$, the reliability of our corrections cannot be determined for this range.

Common to the $C_{24}(\lambda)$–L_{IR} comparisons for the two samples considered is the trend that as one goes to $z \gtrsim 2$ and/or $L_{IR} \gtrsim 10^{12} L_\odot$ the SFRs predict from L_{IR} will be larger than those inferred from the MIR. This may demonstrate that $C_{24}(\lambda)$ is unsuitable when considering galaxies with $\log[L_{IR}/L_\odot] > 12$ or $z \gtrsim 2$, but it could also indicate a change occurs in L_{IR} conversion factor at these luminosities/redshifts. Unfortunately, it is unclear whether what we are observing is a redshift effect or a luminosity effect, as there is a degeneracy between these

variables that cannot be resolved with our current data. In other words, we may simply be seeing a selection effect. Given the higher sensitivity of the *JWST*, would including sources with $L_{IR} \lesssim 12$ at $z \gtrsim 2$ follow the same trend of increasing IR8 when considering the entire population? Prior to the *JWST* mission, a technique that does not rely on L_{IR} to determine SFRs for higher redshift galaxies will be necessary to state confidently what effect is occurring.

7. CONCLUSIONS

We have presented continuous, monochromatic SFR indicators over the mid-IR wavelength range of 6–70 μm, using a sample of 58 SFGs in the SSGSS at $z < 0.2$. The continuous wavelength coverage granted with this sample has allowed for the calibration of *Spitzer*, *WISE*, and *JWST* bands as SFR diagnostics covering, continuously, redshifts from $0 < z < 3$. We find that these diagnostics are consistent with monochromatic calibrations of SFGs in the local universe, and achieve accuracies of 30% or better. They also appear consistent with templates of high-z SFGs, with no significant evidence of variations in the shape of the SED over the 6–30 μm region. Subtle changes of IR8 = $L_{IR}/L_{rest}(8\mu m)$ with redshift appear to cause variations at $z \gtrsim 2$, but currently it is unclear whether this could be due to a selection bias at these redshifts. Due to the significant changes in the FIR region beyond 30 μm with redshift, the use of this region as an SFR diagnostic requires correction to our local template; however, this has been demonstrated to work well up to redshifts of at least $z \sim 1$.

These powerful diagnostics are critical for future studies of galaxy evolution and allows for much easier application to large survey programs with a limited number of MIR wavelength bands. This technique is only valid for SFGs, and therefore methods are required to remove AGNs and SBs from any sample before use. With the upcoming *JWST* mission, we hope that these diagnostics will provide important contributions as we begin to examine more typical MS galaxies up to $z \sim 3$.

REFERENCES

Abazajian, K. N., Adelman-McCarthy, J. K., Agüeros, M. A., et al. 2009, ApJS, 182, 543
Alexander, D. M., Bauer, F. E., Brandt, W. N., et al. 2003, AJ, 126, 539
Armus, L., Mazzarella, J. M., Evans, A. S., et al. 2009, PASP, 121, 559
Assef, R. J., Stern, D., Kochanek, C. S., et al. 2013, ApJ, 772, 26
Baldwin, J. A., Phillips, M. M., & Terlevich, R. 1981, PASP, 93, 5
Béthermin, M., Daddi, E., Magdis, G., et al. 2012, ApJL, 757, L23
Brammer, G. B., van Dokkum, P. G., & Coppi, P. 2008, ApJ, 686, 1503
Brandt, W. N., & Hasinger, G. 2005, ARA&A, 43, 827
Brinchmann, J., Charlot, S., White, S. D. M., et al. 2004, MNRAS, 351, 1151
Brown, M. J. I., Moustakas, J., Smith, J.-D. T., et al. 2014, ApJS, 212, 18
Calzetti, D., Wu, S.-Y., Hong, S., et al. 2010, ApJ, 714, 1256
Calzetti, D. 2013, Secular Evolution of Galaxies ed. J. Falcón-Barroso & J. H. Knapen (Cambridge: Cambridge Univ. Press), 419
Chary, R. R., & Elbaz, D. 2001, ApJ, 556, 562

Ciesla, L., Boquien, M., Boselli, A., et al. 2014, A&A, 565, 128
Cluver, M. E., Jarrett, T. H., Hopkins, A. M., et al. 2014, ApJ, 782, 90
Dale, D. A., & Helou, G. 2002, ApJ, 576, 159
Draine, B. T., & Li, A. 2007, ApJ, 657, 810
Draine, B. T., Dale, D. A., Bendo, G., et al. 2007, ApJ, 663, 866
Draine, B. T., Aniano, G., Krause, O., et al. 2014, ApJ, 780, 172
Dole, H., Rieke, G. H., Lagache, G., et al. 2004, ApJS, 154, 93
Donley, J. L., Koekemoer, A. M., Brusa, M., et al. 2012, ApJ, 748, 142
Donoso, E., Yan, L., Tsai, C., et al. 2012, ApJ, 748, 80
Elbaz, D., Dickinson, M., Hwang, H. S., et al. 2011, A&A, 533, A119
Engelbracht, C. W., Gordon, K. D., Rieke, G. H., et al. 2005, ApJL, 628, L29
Engelbracht, C. W., Rieke, G. H., Gordon, K. D., et al. 2008, ApJ, 678, 804
Glasse, A., Rieke, G. H., Bauwens, E., et al. 2015, PASP, submitted
Gordon, K. D., Engelbracht, C. W., Rieke, G. H., et al. 2008, ApJ, 682, 336
Hao, C.-N., Kennicutt, R. C., Johnson, B. D., et al. 2011, ApJ, 741, 124
Hopkins, A. M., Miller, C. J., Nichol, R. C., et al. 2003, ApJ, 599, 971
Jarrett, T. H., Masci, F., Tsai, C. W., et al. 2013, AJ, 145, 6
Johnson, B. D., Schiminovich, D., Seibert, M., et al. 2006, ApJL, 644, L109
Johnson, B. D., Schiminovich, D., Seibert, M., et al. 2007, ApJS, 173, 392
Juneau, S., Bournaud, F., Charlot, S., et al. 2014, ApJ, 788, 88
Kauffmann, G., Heckman, T., Tremonte, C., et al. 2003, MNRAS, 346, 1055
Kennicutt, R. C. 1998, ARA&A, 36, 189
Kennicutt, R. C., Hao, C.-N., Calzetti, D., et al. 2009, ApJ, 703, 1672
Kennicutt, R. C., Jr, & Evans, N. J., II 2012, ARA&A, 50, 531
Kewley, L., Dopita, M., Sutherland, R., Heisler, C., & Trevena, J. 2001, ApJ, 556, 121
Kewley, L. J., Dopita, M. A., Leitherer, C., et al. 2013, ApJ, 774, 100
Kirkpatrick, A., Pope, A., Alexander, D. M., et al. 2012, ApJ, 759, 139
Komatsu, E., Dunkley, J., Nolta, M. R., et al. 2009, ApJS, 180, 330
Kroupa, P. 2001, MNRAS, 322, 231
Lacy, M., Storrie-Lombardi, L. J., Sajina, A., et al. 2004, ApJS, 154, 166
Lee, J. C., Hwang, H. S., & Ko, J. 2013, ApJ, 774, 62
Le Floc'h, E., Papovich, C., Dole, H., et al. 2005, ApJ, 632, 169
Leitherer, C., Schaerer, D., Goldader, J. D., et al. 1999, ApJS, 123, 3
Lonsdale, C. J., Smith, H. E., Rowan-Robinson, M., et al. 2003, PASP, 115, 897
Lutz, D. 2014, ARA&A, 52, 373
Madau, P., & Dickinson, M. 2014, ARA&A, 52, 415
Madden, S. C., Galliano, F., Jones, A. P., & Sauvage, M. 2006, A&A, 446, 877
Magdis, G. E., Daddi, E., Béthermin, M., et al. 2012, ApJ, 760, 6
Magnelli, B., Elbaz, D., Chary, R. R., et al. 2009, A&A, 496, 57
Marble, A. R., Engelbracht, C. W., van Zee, L., et al. 2010, ApJ, 715, 506
Marchesini, D., van Dokkum, P. G., Förster Schreiber, N. M., et al. 2009, ApJ, 701, 1765
Markwardt, C. B. 2009, adass, 411, 251
Mateos, S., Alonso-Herrero, A., Carrera, F. J., et al. 2012, MNRAS, 426, 3271
Meidt, S. E., Schinnerer, E., Knapen, J., et al. 2012, ApJ, 744, 17
Meidt, S. E., Schinnerer, E., van de Ven, G., et al. 2014, ApJ, 788, 144
Murphy, E. J., Chary, R.-R., Dickinson, M., et al. 2011, ApJ, 732, 126
Murphy, E. J., Condon, J. J., Schinnerer, E., et al. 2011, ApJ, 737, 67
Muzzin, A., Marchesini, D., Stefanon, M., et al. 2013, ApJ, 777, 18
O'Dowd, M. J., Schiminovich, D., Johnson, B. D., et al. 2011, ApJ, 741, 79
Pannella, M., Elbaz, D., Daddi, E., et al. 2014, arXiv:1407.5072
Polletta, M., Tajer, M., Maraschi, L., et al. 2007, ApJ, 663, 81
Rieke, G. H., Alonso-Herrero, A., Weiner, B. J., et al. 2009, ApJ, 692, 556
Salpeter, E. E. 1955, ApJ, 121, 161
Schreiber, C., Pannella, M., Elbaz, D., et al. 2014, arXiv:1409.5433
Shi, F., Kong, X., Wicker, J., et al. 2012, JApA, 33, 213
Somerville, R. S., Gilmore, R. C., Primack, J. R., & Domínguez, A. 2012, MNRAS, 423, 1992
Stern, D., Eisenhardt, P., Gorjian, V., et al. 2005, ApJ, 631, 163
Stern, D., Assef, R. J., Benford, D. J., et al. 2012, ApJ, 753, 30
Tinsley, B. M. 1968, ApJ, 151, 547
Tomczak, A. R., Quadri, R. F., Tran, K.-V. H., et al. 2014, ApJ, 783, 85
Tremonti, C. A., Heckman, T. M., Kauffmann, G., et al. 2004, ApJ, 613, 898
Treyer, M., Schiminovich, D., Johnson, B. D., et al. 2010, ApJ, 719, 1191
U, V., Sanders, D. B., Mazzarella, J. M., et al. 2012, ApJS, 203, 9
Wright, E. L., Eisenhardt, P. R. M., Mainzer, A. K., et al. 2010, AJ, 140, 1868
Zhu, Y.-N., Wu, H., Cao, C., & Li, H.-N. 2008, ApJ, 686, 155